Chapter 4

Coupled Climate Model

Simplify, simplify.

Thoreau, *Walden*

4.1 Rationale

To ensure the robustness and usefulness of this study, a wide range of climates and model parameters must be explored. A coupled general circulation model would be too costly for this task, both conceptually and computationally. We therefore simplify the dynamics to retain only the processes most relevant to the tropical Pacific climatology and ENSO. Intermediate models, like the one developed in this chapter, have been used extensively over the past decade to construct a vocabulary for ENSO dynamics (see Neelin et al., 1998, for a review). The behaviors found in such models provide essential prototypes for those found in more complex models and in observations. Intermediate models may therefore be viewed as stepping stones to a more complete understanding of tropical climate dynamics.

The use of an intermediate model involves a trade-off between realism and control. Processes such as mixing, clouds, and evaporation are heavily parameterized, so results from the model must necessarily be viewed with caution until verified by more realistic simulations or observations. However, the conceptual and computational efficiency of such a model offers several great advantages. First, it affords the experimenter a large degree of control over the dynamics, which allows hypotheses to be tested cleanly and easily. Second, its computational efficiency provides great freedom for exploration, which allows a wider variety of hypotheses to be tested, and tested more carefully, than would be possible in a GCM. Finally, the simplicity of an intermediate model allows its essential behavior to be understood completely, free from complications arising from secondary processes.

For the purpose of mapping a vast climate parameter space, and translating this map into a physical understanding of ENSO, the benefits of a simplified model here seem to outweigh the costs. The analysis and mapping of intermediate models are further motivated by the need to unify, and put into proper context, the large body of existing literature

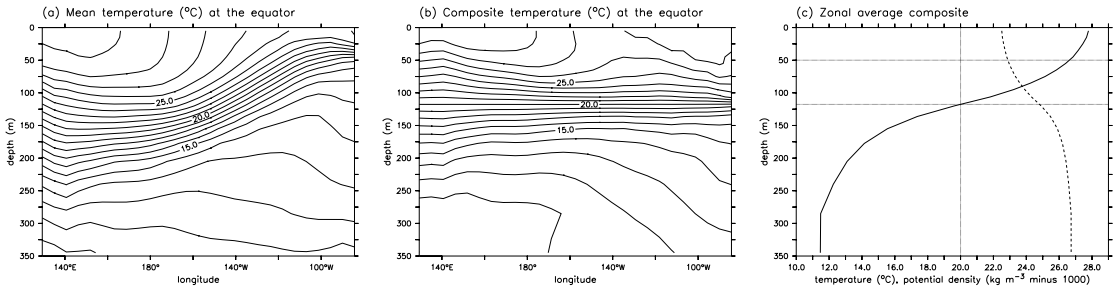

Figure 4.1: Observed vertical thermal structure of the equatorial band (2°S–2°N) during the 1980–1999 period, from the analysis of Behringer et al. (1998). (a) Mean temperature. (b) Composite temperature, obtained as a time average of instantaneous profiles which have been vertically shifted so that their 20°C isotherm lies at the time-mean, zonal-mean depth of the 20°C isotherm. (c) Zonal average composite temperature (solid) and potential density (dashed). Potential density is estimated from the UNESCO equation of state, assuming a reference pressure of 1010 mb and a salinity of 35 parts per thousand.

on such models. The analysis will also be directly applicable to at least some current operational predictions, since intermediate models are still being used for this purpose (Chen et al., 1999).

4.2 Ocean model

4.2.1 Governing equations

Active layer

To a first approximation, the vertical structure of the equatorial Pacific ocean consists of a nearly homogeneous mixed layer near the surface, a sharp thermocline at depth, and a deep bottom layer (Fig. 4.1). A reasonable idealization is a fluid consisting of two vertically-homogeneous layers, with no mixing or friction between the layers. If the bottom layer is assumed to be motionless and infinitely deep, then no horizontal pressure gradients can develop in that layer, and pressure gradients induced by the slope of the sea surface must exactly cancel those induced by the slope of the thermocline. The slope of the thermocline must then be proportional and opposite to the slope of the sea surface.

The average density of active layer is only slightly less than that of the bottom layer, so density variations may be neglected in the equations of motion except where they give rise to pressure gradients (the Boussinesq approximation). Also, because the relative density difference between cold and warm water is much smaller than that between water and air, variations in thermocline slope will be much greater than variations in sea surface height. Surface height variations will therefore play little role in the mass balance of the active layer, and can be neglected in this respect (the rigid lid approximation). Although the surface variations *are* essential for generating pressure gradients within the active layer, these effects can be parameterized in terms of the thermocline slope as noted above.

Let h_1 denote the linear departure of the active (upper) layer depth from its constant reference depth H, and let $\mathbf{U}_1 \equiv (U_1, V_1)$ denote the vertically-integrated horizontal transport of water within the active layer. Restricting attention to long-wave, near-geostrophic flows (wavelengths $\gg$ 300 km, times $\gg$ 1 day), and integrating vertically over the active layer, the linearized equations for conservation of momentum and mass are given by the *longwave reduced gravity model*

$$\partial_t U_1 = f V_1 - c^2 \partial_x h_1 + \frac{\tau_x}{\rho} - r U_1 \tag{4.1}$$

$$0 = -f U_1 - c^2 \partial_y h_1 + \frac{\tau_y}{\rho} - r V_1 \tag{4.2}$$

$$\partial_t h_1 = -\boldsymbol{\nabla} \circ \mathbf{U}_1 - r h_1 \tag{4.3}$$

where $f = \beta y$ is the equatorial beta-plane approximation to the Coriolis parameter, ρ is the seawater density, r is the dissipation coefficient for mass and momentum, $c^2 = g'H$ is the squared speed of internal gravity waves, $g' = g\Delta\rho/\rho$ is the reduced gravity, and τ_x and τ_y are the zonal and meridional components of the surface wind stress. Note that $\partial_t V_1$ has been eliminated from (4.2) by the assumption of low frequencies and large zonal scales.

The boundary conditions for (4.1)–(4.3) are as follows. There is assumed to be no flow through the northern and southern boundaries. The eastern and western boundaries in reality are thought to be leaky, since they are not perfectly meridional and the western boundary has gaps (Clarke, 1991; Mantua and Battisti, 1994; Kang and An, 1998; Boulanger and Menkes, 1999; Thompson and Battisti, 2000). At the eastern boundary, only a fraction R_e of the zonal transport associated with the impinging Kelvin wave signal is canceled by the generation of long Rossby waves through boundary reflection. Similarly at the western boundary, only a fraction R_w of the zonal transport associated with the impinging Rossby wave signal is canceled by the generation of equatorial Kelvin waves through boundary reflection. In the west, there is a narrow boundary layer where short Rossby waves act to redistribute mass meridionally, and since the long-wave approximation has eliminated short Rossby waves from (4.1)–(4.3), the appropriate western boundary condition must be formulated in terms of the meridionally integrated flow (Cane and Sarachik, 1977). Points close to the model's artificial north/south boundaries will be contaminated by spurious coastal Kelvin waves, so these points are neglected from the flow integral (Battisti, 1988). In summary, the boundary conditions for (4.1)–(4.3) are formulated as

$$V_1 = 0 \quad \text{at} \quad y = y_s,\, y_n \tag{4.4}$$

$$U_{1,Rossby} = -R_e U_{1,Kelvin} \quad \text{at} \quad x = x_e \tag{4.5}$$

$$\int_{y_s}^{y_n} U_{1,Kelvin}\, dy = -R_w \int_{y_s + L(y_s)}^{y_n - L(y_n)} U_{1,Rossby}\, dy \quad \text{at} \quad x = x_w \tag{4.6}$$

where $L(y) = c(\beta y)^{-1}$ is the coastal radius of deformation at latitude y, and $U_{1,Kelvin}$ and $U_{1,Rossby}$ are the Kelvin and Rossby components of the active layer zonal transport.

At the equator and in the limit of no damping, the steady-state thermocline slope is in balance with the zonal wind stress: $\rho g' H \partial_x h_1 = \tau_x$. This implies that the eastern Pacific will be an important dynamical region for ENSO for two reasons. First, the prevailing

easterly trade winds induce a slope in the thermocline, such that it shoals in the eastern Pacific; the presence of strong vertical temperature gradients near the surface in the east then makes vertical entrainment in this region very sensitive to variations in upwelling and thermocline depth. Second, the eastern Pacific is a region of strong vertical motions of the thermocline, since it is impacted by the full force of the zonal wind fetch integrated across the basin. It is this combination of strong *sensitivity* to thermocline depth and strong *activity* of thermocline motions that make the eastern Pacific a key region in the cycle of coupled feedbacks responsible for ENSO.

Given the importance of the thermocline depth in the eastern equatorial Pacific, a special problem then arises due to the linearity of (4.1)–(4.3). If the thermocline depth anomalies are not small compared to the active layer depth, then a more appropriate steady-state zonal balance is $\rho g'(H+h)\partial_x h = \tau_x$ where h denotes the thermocline depth anomaly in nonlinear balance. Comparing this to the linear balance gives $\partial_x h_1 = (1 + h/H)\partial_x h$, which indicates that $\partial_x h_1$ will underestimate the thermocline slope where h is negative, i.e. where the thermocline is shallower than H. This will be the case in the eastern Pacific, where the thermocline is shallow due to the prevailing easterly trade winds.

To improve the thermocline depth simulation in the east Pacific, we therefore introduce scaled versions of the linear thermocline depth and active layer transport for use by the mixed layer model:

$$h = \lambda_h h_1 \tag{4.7}$$

$$\mathbf{U}_{al} = \lambda_u \mathbf{U}_1 \tag{4.8}$$

The coefficients λ_h and λ_u are chosen so that the simulated h (especially in the east Pacific) and $\mathbf{U}_{al}$ (especially in the central Pacific) best agree with observations.

Mixed layer currents

The cold tongue is maintained largely by vertical entrainment of cold water into the mixed layer. This entrainment can be simulated by embedding an Ekman layer into the top of the active layer, following Zebiak and Cane (1987). We assume the wind stress forcing is deposited entirely within a layer of constant depth H_m, so that the total transport in the active layer is given by

$$\mathbf{U}_{al} = \mathbf{U} + \mathbf{U}_i \tag{4.9}$$

where $\mathbf{U}_{al} \equiv H\mathbf{u}_{al}$ is the active layer transport, $\mathbf{U} \equiv H_m\mathbf{u}$ is the mixed layer transport, and $\mathbf{U}_i \equiv (H - H_m)\mathbf{u_i}$ is the interior (non-mixed layer) transport in the active layer. The vertical-average currents in the active layer, mixed layer, and interior layer are denoted by $\mathbf{u}_{al}$, $\mathbf{u}$, and $\mathbf{u}_i$, respectively.

Continuity gives the upwelling velocity at the base of the mixed layer:

$$w = \boldsymbol{\nabla} \circ \mathbf{U} \tag{4.10}$$

Assuming the active layer has uniform density, the pressure gradients in the interior active layer must be the same as those in the mixed layer. The extra flow in the mixed layer which

is not present in the interior must be due to the frictional (Ekman) transport, denoted by

$$\mathbf{U}_s \equiv H_m \mathbf{u}_s \tag{4.11}$$
$$\mathbf{u}_s \equiv \mathbf{u} - \mathbf{u}_i \tag{4.12}$$

Assuming the vertical current structure is in equilibrium with the wind stress, subtracting the momentum equations for the interior active layer from those of the mixed layer gives the shear equations

$$0 = fV_s + \frac{\tau_x}{\rho} - r_s U_s \tag{4.13}$$
$$0 = -fU_s + \frac{\tau_y}{\rho} - r_s V_s \tag{4.14}$$

or

$$\mathbf{U}_s = \frac{r_s \boldsymbol{\tau} - f\hat{k} \times \boldsymbol{\tau}}{\rho\left(f^2 + r_s^2\right)} \tag{4.15}$$

The coefficient r_s, which controls the viscosity of the mixed layer, strongly affects the equatorial upwelling response to wind stress (Appendix C).

Finally, the mixed layer currents and transports are obtained from the transport budget (4.9):

$$\mathbf{u} = \mathbf{u}_{al} + \left(1 - \frac{H_m}{H}\right)\mathbf{u}_s \tag{4.16}$$
$$\mathbf{U} = \mathbf{U}_s + \frac{H_m}{H}\left(\mathbf{U}_{al} - \mathbf{U}_s\right) \tag{4.17}$$

In summary, the mixed layer transport consists of the Ekman transport plus the fraction of buoyancy-driven transport that occurs within the mixed layer.

Thermodynamics

The model mixed layer is assumed to have uniform temperature in the vertical, i.e. the vertical-average mixed layer temperature is assumed equivalent to SST. The mixed layer temperature equation includes three-dimensional nonlinear advection, horizontal mixing represented by a diffusion term, and surface heat flux represented by linear damping of SST:

$$\partial_t T = -u\partial_x T - v\partial_y T - \mathcal{R}(w)\partial_z T + \kappa\nabla^2 T - \epsilon\left[T - T_0(y)\right] \tag{4.18}$$

where κ is the eddy diffusivity, ϵ is the damping rate, and $\mathcal{R}$ is the ramp function

$$\mathcal{R}(x) \equiv \begin{cases} 0 & : \quad x \le 0 \\ x & : \quad x > 0 \end{cases} \tag{4.19}$$

$T_0(y)$ is the equilibrium surface temperature in the absence of ocean dynamics; it is assumed to have a parabolic structure in the meridional, with a peak at the equator:

$$T_0 = T_0(y = 0) - ay^2 \tag{4.20}$$

Table 4.1: Ocean model grid parameters: minimum and maximum coordinates, spacing, and number of points in longitude and latitude.

Field	x_w	x_e	Δx	n_x	y_s	y_n	Δy	n_y
mixed layer u,v,w,T	129.375°E	84.375°W	5.625°	27	19°S	19°N	2°	20
active layer u_1,h_1	124°E	80°W	2°	79	28.50°S	28.50°N	0.5°	115
active layer v_1	125°E	81°W	2°	78	28.75°S	28.75°N	0.5°	116

The effective vertical entrainment temperature gradient $\partial_z T$ is

$$\partial_z T \equiv \frac{\gamma(T - T_e)}{H_m} \tag{4.21}$$

where γ is the entrainment efficiency. The temperature T_e of water entrained into the mixed layer at depth H_m is parameterized in terms of the thermocline depth h:

$$T_e = T_c + \delta \left[e^{(h-H_m)\Gamma/\delta} - 1 \right] \tag{4.22}$$

$$\delta \equiv T_c - \begin{cases} T_{min} & : \quad h \le H_m \\ T_{max} & : \quad h > H_m \end{cases} \tag{4.23}$$

Direct buoyancy effects of mixed layer temperature changes on the active layer pressure gradients are assumed to be small and are ignored. Changes in SST, however, will feed back indirectly on the ocean dynamics through the wind stress forcing.

4.2.2 Numerics

The horizontal grids for the ocean model are shown in Table 4.1 and Fig. 4.2. Both the active layer and mixed layer models assume a rectangular ocean basin. To adequately resolve equatorial waves, the ocean dynamics are computed on a dense grid, with the meridional velocity grid staggered in x and y relative to the zonal velocity and depth grids to give second order accuracy in space. The mixed layer fields are computed on a lower resolution grid.

The active layer equations (4.1)–(4.3) are integrated forward in time using the method of Cane and Patton (1984). The "Kelvin wave" part of the solution is propagated eastward using the method of characteristics, while the remaining "Rossby wave" part of the solution is propagated westward numerically using an implicit scheme centered in time. In combination with the staggered ocean dynamics grid, this method provides second-order accuracy in time and space and conserves mass and energy away from boundaries. While there are fluxes of mass and energy through the boundaries, these are small and acceptable for our purposes. The great advantage of this scheme is that it allows a very long timestep of 10 days to be used with good accuracy.

Active-layer fields are averaged onto the coarse mixed layer grid prior to the advection computation. After adding the Ekman contribution to the mixed layer currents, the upwelling is computed from (4.10) using centered differences. At the western, southern, and northern boundaries, upwelling is set equal to that computed at the nearest interior point.

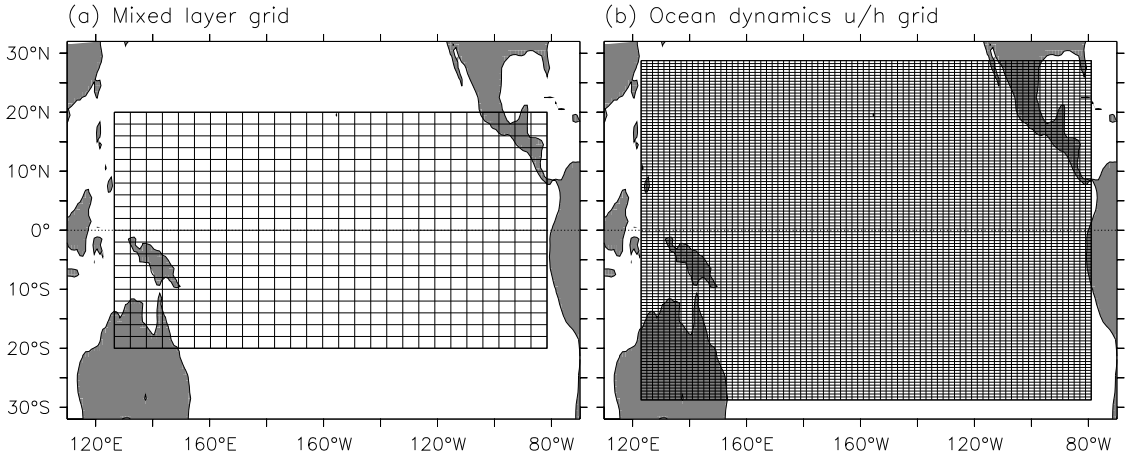

Figure 4.2: Spatial domains and grid boxes for the ocean model. (a) Mixed layer grid boxes for temperature, horizontal velocity, and upwelling. (b) Active layer grid boxes for thermocline depth and zonal velocity; meridional velocity gridpoints are centered at the corners of these boxes. Continents are shown for scale only; the model assumes a rectangular basin.

At the eastern boundary, a boundary condition of no normal flow is assumed in order to simulate coastal upwelling observed off the coast of Peru.

With the currents and thermocline depth fields in hand, the mixed layer temperature tendency equation (4.18) is then integrated forward in time using first-order time-differencing and upwind advection, with no advective flux allowed through model boundaries. At each time step, the upwind direction is determined from the *total* velocity field. This differs slightly from the approach of Zebiak (1985), who simply used the climatological or anomalous velocity field (depending on which advective term was being evaluated) to determine the upwind direction. In the present model, the total velocity sets the upwind direction for every term, giving both a more physically consistent advective scheme and more linear behavior at small amplitudes as expected. The advective scheme is rather dissipative of temperature anomalies at scales comparable to the grid spacing. This dissipation can be considered an implicit horizontal mixing term, which is comparable in magnitude to the explicit mixing included in (4.18). Two nice properties of the advective scheme are that it does not generate artificial temperature anomalies on its own, and it advects temperature anomalies at a speed very close to the true advective speed. In order to ensure numerical stability, the advective timestep adjusts automatically to the speed of the mixed-layer currents and the strength of the horizontal dissipation; the advective timestep is typically on the order of 2–3 days.

4.2.3 Calibration

Observations, models, and theories of ENSO have improved considerably since the pioneering work of Zebiak and Cane (1987). Although some limitations of the original version of the model have been pointed out, subsequent studies have shown that reformulating and

Table 4.2: Ocean model parameters and their standard values.

Parameter	Symbol	Value
	Active layer	
density of surface seawater	ρ	1023 kg m^{-3}
thermocline stratification	$\Delta\rho/\rho$	0.005
observed active layer depth	H_{obs}	124 m
resting active layer depth	H_0	143 m
active layer dissipation	r	(18 months)$^{-1}$
western boundary reflectivity	R_w	0.85
eastern boundary reflectivity	R_e	0.85
thermocline depth coefficient	λ_h	1.7
transport coefficient	λ_u	1.0
	Mixed layer	
mixed layer depth	H_m	50 m
vertical shear dissipation	r_s	(2 days)$^{-1}$
horizontal eddy diffusivity	κ	4000 m^2 s^{-1}
surface flux coefficient	ϵ	20 W m^{-2} K^{-1}
equatorial equilibrium SST	$T_0(y=0)$	30°C
y-curvature of $T_0(y)$	a	0.0125 K (°lat)$^{-2}$
	Entrainment parameterization	
entrainment efficiency	γ	0.75
thermocline central temperature	T_c	20°C
minimum T_e	T_{min}	16°C
maximum T_e	T_{max}	30°C
maximum $\partial_h T_e$	Γ	0.17 K m^{-1}

retuning the model can greatly improve its performance (Chang, 1994; Mantua and Battisti, 1995; Wang, 1995; Perigaud and Dewitte, 1996; Dewitte and Perigaud, 1996; Perigaud et al., 1997, 2000a; Cassou and Perigaud, 2000). In addition, although the model was not originally designed to simulate the tropical climatology, Seager et al. (1988) showed that the ocean model framework can successfully reproduce many aspects of this climatology as long as realistic surface fluxes are supplied. The present section builds on this past work by formulating a consistent parameter set that can be used to simulate both the tropical Pacific climatology and ENSO. This motivates a careful comparison of the model simulations against recent observations, and requires a thorough re-tuning of the ocean model. Resulting parameter values for the control run are given in Table 4.2.

Active layer

The linear reduced gravity system (4.1)–(4.3) has four free parameters: the internal gravity wave speed c, the dissipation r, and the boundary reflection coefficients R_e and R_w. The value of c controls the speed of the ocean adjustment to changes in wind stress. Observations suggest that over recent decades, c has been in the range of 2 to 3 m s^{-1} (McPhaden et al., 1998; Neelin et al., 1998), and eigenanalyses of the observed density structure of the ocean indicate first baroclinic mode speeds ranging from 2.4 to 2.9 m s^{-1} and second baroclinic mode speeds ranging from 1.4 to 1.8 m s^{-1} (Busalacchi and O'Brien,

1981; Cane, 1984; Philander, 1990). Intermediate models have typically assumed c to be around 2.9 m s^{-1} (Zebiak and Cane, 1987; Battisti, 1988). Kleeman (1993) tried a range of speeds in a coupled intermediate model and found the best hindcast skill was achieved with c between 2.2 and 2.4 m s^{-1}, i.e. at speeds intermediate between the first and second baroclinic modes. In this study, c must be allowed to vary with H, since effects of changes in the basic state are being tested. We therefore fix the stratification $\Delta\rho/\rho$ at the constant value that gives $c = 2.5$ m s^{-1} when H is set equal to H_{obs}, the observed thermocline depth averaged over the latitudes of strong wave propagation (8°S–8°N). Using the Behringer et al. (1998) ocean analysis for the 1980–1999 period and approximating the thermocline depth by the depth of the 20°C isotherm, we obtain the values given in Table 4.2.

The active-layer dissipation parameter, r, plays a central role in the generation of steady-state currents in response to the climatological wind stress (Yamagata and Philander, 1985). Zebiak and Cane (1987) and Battisti (1988) assumed a rather small value of $r = (30 \text{ months})^{-1}$, which provided a good simulation of the climatological currents and off-equatorial thermocline depth. As pointed out by Mantua and Battisti (1995), however, the single-mode reduced gravity system traps too much energy near the surface, resulting in a basin resonance at periods of 9–11 months (corresponding to a Kelvin wave/Rossby wave circuit) that is much stronger than observed. In a continuously stratified ocean, equatorial waves propagate energy downward and out of the surface layer (Philander, 1990). To represent this process, a few authors have suggested increasing the value of r to $(12 \text{ months})^{-1}$ or more (Picaut et al., 1993; Perigaud and Dewitte, 1996; Thompson and Battisti, 2000). However, if r is too strong then the simulation of the climatological currents and thermocline depth suffers. We therefore choose a value $r = (18 \text{ months})^{-1}$, which is strong enough to attenuate the spurious high-frequency basin-resonant mode but weak enough to give a decent simulation of the off-equatorial climatology.

The boundary reflection coefficients R_e and R_w control the mass flux through the eastern and western boundaries. During a warm event, for example, equatorial westerly stress anomalies generate a Kelvin wave depression in the equatorial thermocline, which propagates eastward. The off-equatorial cyclonic stress curl associated with the equatorial westerlies also generates a Rossby wave elevation in the off-equatorial thermocline, which propagates westward. Both the Kelvin and Rossby signals are associated with eastward equatorial currents. At the eastern and western boundaries, the currents are partially canceled by the generation of reflected waves. The part of the impinging signal that is not canceled (due to imperfect reflection) corresponds to a mass flux through the boundary.

As discussed by An and Kang (2000), this boundary flux is important for controlling the zonal-mean thermocline depth response to changes in wind stress. Depending on the strength of the boundary reflections, the boundary fluxes can act to enhance or inhibit the shoaling of the equatorial zonal-mean thermocline brought about by geostrophic divergence in the interior. For a downwelling Kelvin wave, an imperfect reflection at the *eastern* boundary results in an eastward mass flux *out of* the equatorial band, which helps to *shoal* the equatorial thermocline and *cool* SST through vertical advection. In the presence of a westward background SST gradient, however, the eastward mass flux tends to *warm* SST through zonal advection. The net effect of the eastern boundary flux is therefore a competition between zonal and vertical advective processes. A decrease in R_e can either

lengthen the ENSO period (if the zonal advection effect dominates) or shorten the period (if the vertical advection effect dominates).

Imperfect reflection at the *western* boundary, on the other hand, results in eastward mass flux *into* the equatorial band through that boundary, which serves to *deepen* the equatorial thermocline. In this case, both zonal advection and vertical advection act as a positive feedback on SST anomalies. This delays termination of an event, by counteracting the cooling by equatorial discharge induced by cyclonic off-equatorial wind stress curl. As a result, a decrease in R_w will tend to lengthen the oscillation period. If R_w is so weak that the western boundary flux overwhelms the geostrophic divergence, then the system will no longer oscillate and will instead drift to a new equilibrium.

The actual boundary reflectivities are difficult to estimate, due to the complexity of the coastal geometry and bathymetry. The reflectivity is sensitive not only to the shape and continuity of the boundary, but also to the frequency of the reflecting wave signals. A recent observational estimate of R_e places it around 0.75 (Boulanger and Menkes, 1999). Theoretical estimates of R_w are in the vicinity of 0.8-0.9 (Clarke, 1991; du Penhoat and Cane, 1991), while observational estimates range from 0.7 (Mantua and Battisti, 1994) to nearly 1.0 (Boulanger and Menkes, 1999). Intermediate models have used different values for the reflection coefficients. Zebiak and Cane (1987) and Battisti (1988) assumed perfect reflections at both boundaries; Thompson and Battisti (2000) recommended $R_e = 1.0$, $R_w = 0.7$; Kang and An (1998) and An and Kang (2000) used $R_e = R_w = 0.7$. Experiments with the present model suggest that $R_e = R_w = 0.85$ gives a good simulation of the relative amplitude and phasing of the zonal thermocline slope and zonal-mean thermocline depth. As these values are in the middle of the range of reflectivities suggested by previous work, we adopt them into the standard model (Table 4.2).

Next, a value of λ_h is chosen to optimize the simulation of thermocline depth. For this purpose, H is set equal to H_{obs} and the active layer model is forced with the FSU wind stress anomalies over the 1980–1999 period. Figs. 4.3 and 4.4 show that for the standard value of λ_h in Table 4.2, the model gives a decent simulation of the equatorial thermocline depth anomalies. The amplitude of the thermocline response to the stress appears to be correct, both for the zonal slope and the zonal mean across the basin. That the FSU-forced simulation is poor during 1984–1986 and 1996 may result from problems with the FSU stress product (Chapter 2), perhaps amplified by the basin resonance noted earlier. (Note that forcing the model instead with the NCEP stress anomalies gives a much better simulation during these periods.) Due to the linearity of the model, the simulated thermocline depth variability in the western Pacific is too strong, but this is of little concern since the thermocline is deep in that region and therefore should play little role in directly affecting surface temperatures.

The tropical Pacific surface current variability is less well known than the thermocline depth variability. We expect that $\lambda_u = 1$ should be appropriate, since the equatorial zonal current anomalies are most active in the central and western Pacific where the thermocline depth is not far from H. A comparison of the simulated active-layer current anomalies with measurements reported in the literature (Lagerloef et al., 1999; Wang, 2000b; Wang and McPhaden, 2001; Grodsky and Carton, 2001) indicates that $\lambda_u = 1$ is indeed reasonable, so we adopt this value into the standard model.

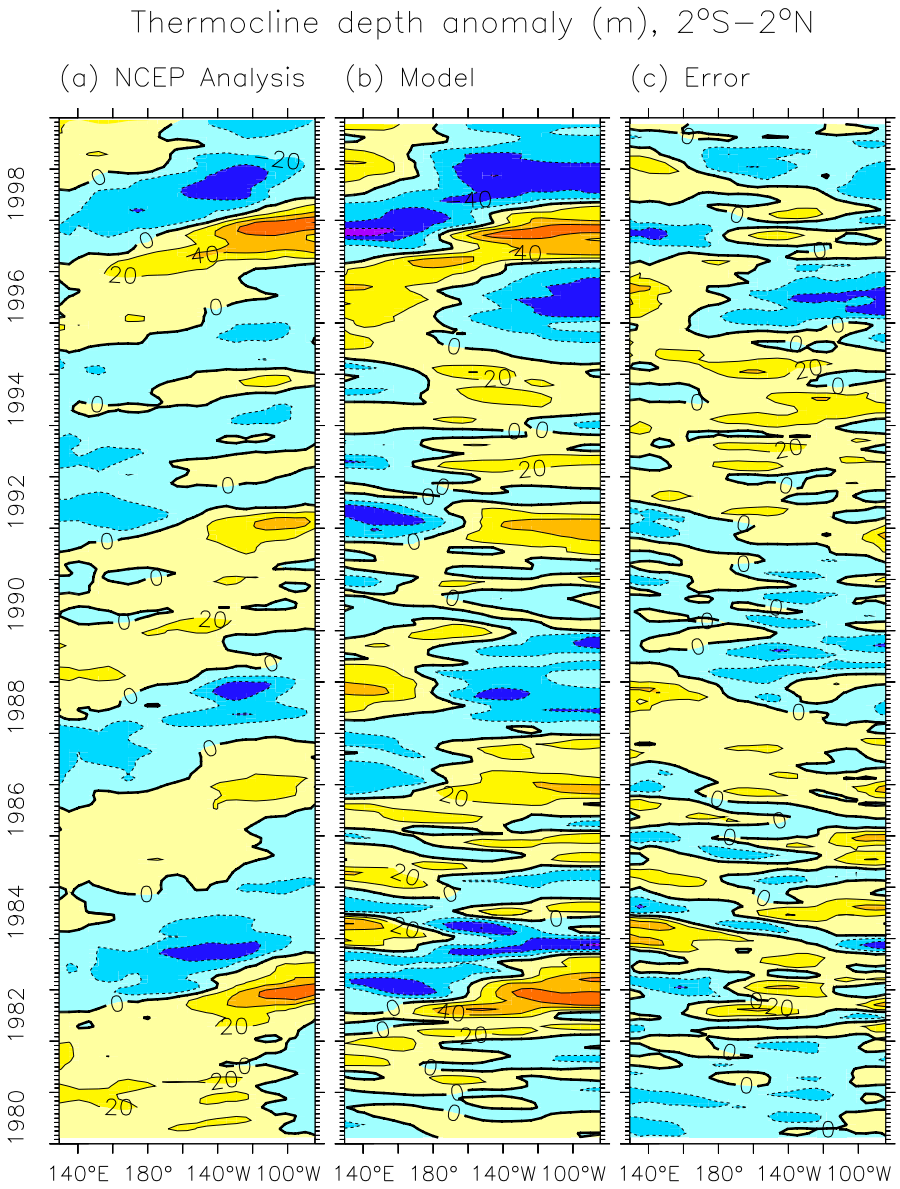

Figure 4.3: Thermocline depth anomaly (m) along the equator, averaged over 2°S–2°N and smoothed with a 3-month triangle filter. (a) Anomalous depth of the 20°C isotherm from the observational analysis of Behringer et al. (1998). (b) Anomalous thermocline depth from the standard active layer model forced by observed FSU stress anomalies. (c) Depth error, model minus observations.

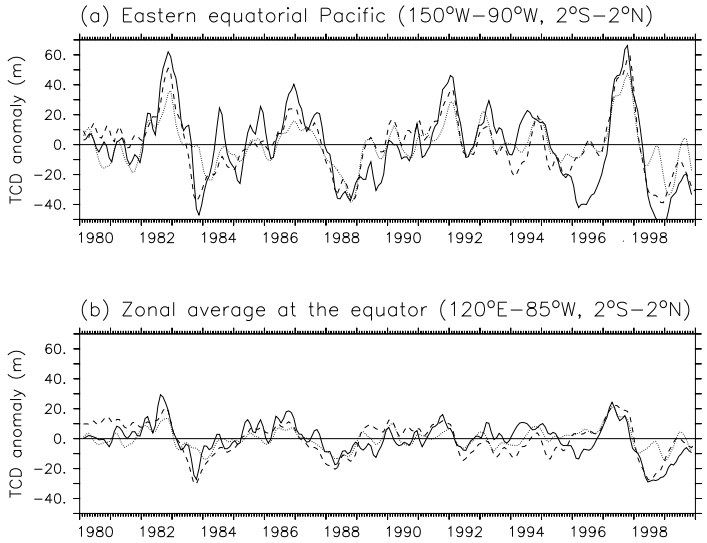

Figure 4.4: Thermocline depth anomaly (m) along the equator, averaged over 2°S–2°N and zonally across the (a) eastern basin, and (b) full basin. Anomalies have been smoothed with a 3-month triangle filter. Dashed line is the 20°C isotherm from the observational analysis of Behringer et al. (1998). Solid line is the standard model forced by FSU stress anomalies, dotted line is forced by NCEP stress anomalies.

Finally, a value for H_0, the thermocline depth in the absence of any wind stress forcing, must be chosen to optimize the simulation of the climatological thermocline depth. The overriding goals for the climatology are (1) a realistic thermocline depth in the eastern Pacific, and (2) a realistic average thermocline depth over the latitudes of strong wave propagation (8°S–8°N). To this end, the model is spun up with the FSU climatological wind stress using various values of H_0. Fig. 4.5 shows that the standard value of H_0 in Table 4.2 results in both a realistic equatorial thermocline depth and a value of H very close to H_{obs}.

Mixed layer currents

The mixed layer has two parameters: a constant depth H_m and a viscosity r_s. Fig. 4.6 shows that in reality, the mixed layer depth varies substantially with location and time. Along the equator, the mixed layer is much shallower in the eastern Pacific than in the central and western Pacific. The equatorial mixed layer is deepest in boreal winter and during El Niño, and shallowest in boreal spring and during La Niña. Clearly a model with a fixed-depth mixed layer may not adequately represent the entrainment processes going on in the real world. Inclusion of a fully interactive mixed layer, however, would complicate the analysis considerably. We instead proceed with the constant-depth mixed layer formulation that has met with much success in understanding and predicting ENSO. Fig. 4.6 indicates that the time-average, zonal-average mixed layer depth near the equator is very close to 50 m (the standard value used by Zebiak and Cane (1987)), so we adopt

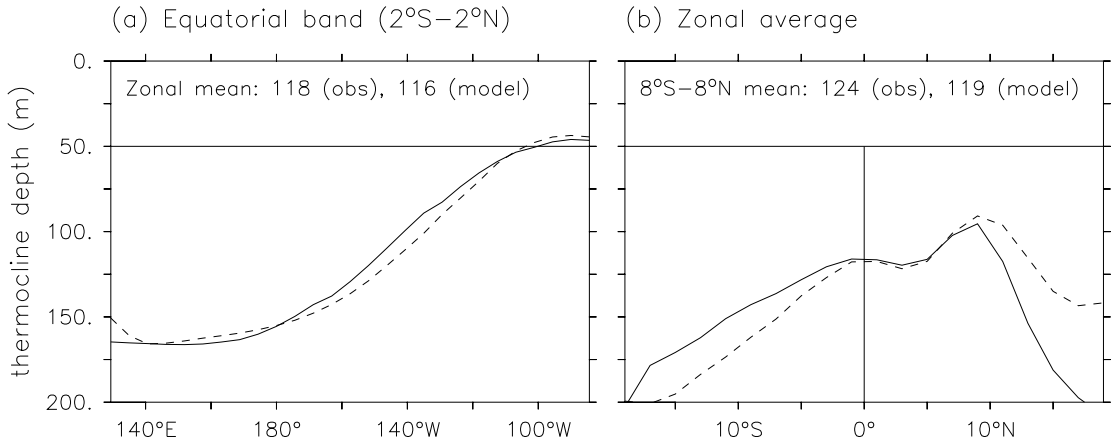

Figure 4.5: Climatology of thermocline depth (m) for the 1980–1999 period. Dashed line is the 20°C isotherm from the observational analysis of Behringer et al. (1998). Solid line is the thermocline depth simulated by the standard model when forced by the climatological FSU stress. (a) Meridional average over the equatorial band, 2°S–2°N; label indicates the zonal mean values over the entire basin. (b) Zonal average over the entire basin; label indicates the meridional means over 8°S–8°N.

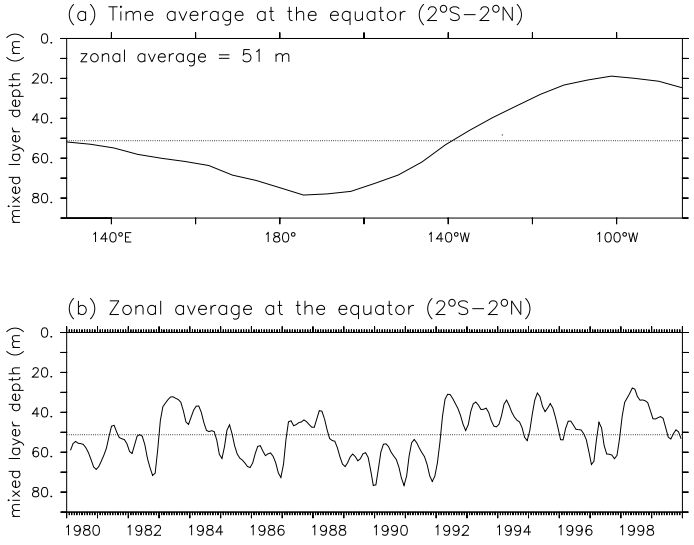

Figure 4.6: Observed mixed layer depth (m), defined as that depth which is 0.5°C cooler than the surface, from the analysis of Behringer et al. (1998). Data are averaged over 2°S–2°N for the 1980–1999 period. (a) Time average. (b) Zonal average over the entire basin. Dotted lines indicate the zonal/time average mixed layer depth, which is labeled in (a).

this value for H_m.

As shown in Appendix C, the mixed layer viscosity r_s controls the intensity and structure of the frictional surface circulation (Ekman flow). Since the upwelling strength is extremely important to the coupled dynamics of the climatology and ENSO, it will be the primary constraint in choosing a value for r_s. For nondivergent winds, (C.8) gives

$$r_s^2 = -\frac{H - H_m}{\rho H} \frac{\beta \tau_x}{w(y=0)} \tag{4.24}$$

The actual mean upwelling along the equator in the Pacific is difficult to estimate. It arises from a divergence of surface currents, so it is highly prone to errors in those currents. Also, because the strongest upwelling occurs in a narrow band near the equator and exhibits large spatial and temporal variability, the data are subject to sizable aliasing and interpolation errors. Weisberg and Qiao (2000) review a number of techniques that have been brought to bear on this problem. A recent estimate by Meinen et al. (2001) suggests that the annual-mean climatological vertical velocity across 50 m depth is 0.28 ± 0.03 m day^{-1} averaged over the region 155°W–95°W, 5°S–5°N. Johnson et al. (2001) obtain a larger value of 0.66 ± 0.19 m day^{-1} averaged over 170°W–95°W, 3.6°S–5.2°N, with a peak zonally-averaged equatorial upwelling velocity of 1.6 ± 0.8 m day^{-1}.

To estimate r_s in the intermediate model, we first average the FSU observed equatorial zonal stress over 170°W–95°W to get $\tau_x = -0.5$ dPa $= -3.73 \times 10^8$ kg m^{-1} day^{-2}. Assuming $H = 125$ m, $H_m = 50$ m, $\rho = 1023$ kg m^{-3}, $\beta = 1.97 \times 10^{-6}$ (m day)$^{-1}$, $w(y=0) = 1.6$ m day^{-1}, equation (4.24) gives $r_s = (1.9 \text{ days})^{-1}$. Note that there is a fair amount of uncertainty in this parameter, given the large error bars on the observational estimate, and the coarse resolution of the mixed layer model (the closest equatorial points are at 1°S and 1°N). The estimated value is close enough to the $(2.0 \text{ days})^{-1}$ used in the Zebiak and Cane (1987) model that we simply adopt the latter value. Forcing the full model (including the shallow water component) with the seasonally-varying climatology of FSU vector wind stress from the 1980–1999 period, gives annually-averaged, spatially-averaged simulated upwelling velocities of 0.43 m day^{-1} over 170°W–95°W, 3.6°S–5.2°N; 1.02 m day^{-1} over 170°W–95°W, 2°S–2°N; and 0.39 m day^{-1} over 155°W–95°W, 5°S–5°N. These values are in the midrange of current observational estimates.

Thermodynamics

The entrainment temperature parameterization is plotted along with observations in Fig. 4.7. T_e increases smoothly with thermocline depth from T_{min} to T_{max}, passing through the inflection point (H_m, T_c) where the maximum $\partial_h T_e$ of Γ occurs. The value of T_c is set to 20°C, which is a good fit to the thermocline central temperature along the equator. The entrainment temperature can get no warmer than T_{max}, which is set to the equatorial equilibrium temperature $T_0(y=0)$, and no colder than T_{min}, which is set to 16°C to prevent excessive cooling in the eastern equatorial pacific during La Niña, when the 20°C isotherm tends to outcrop due to the linearity of the reduced gravity model. The slope of the parameterization at (H_m, T_c), controlled by the parameter Γ, is calibrated by performing a least-squares optimization using 240 months of observed 50 m temperature sections for the 1980–1999 period from the analysis of Behringer et al. (1998).

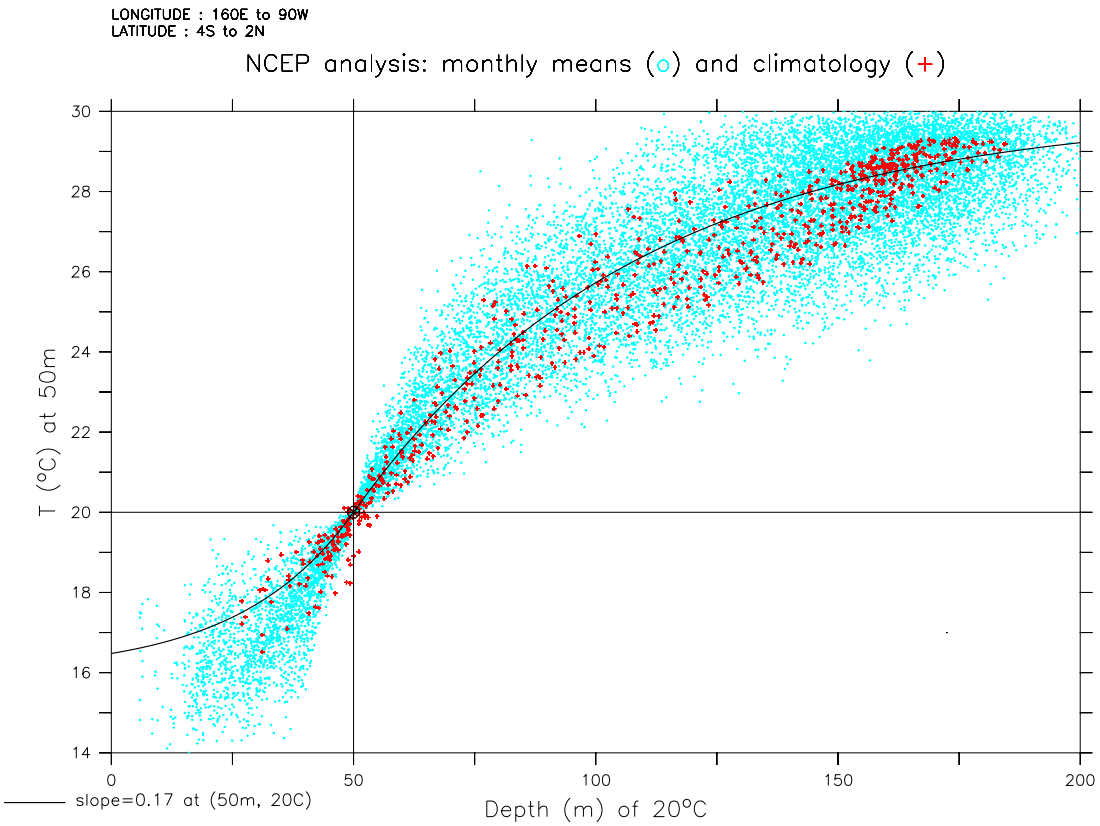

Figure 4.7: Temperature at 50 m depth, versus the depth of the 20°C isotherm, over the region 160°E–90°W, 4°S–2°N. Dots indicate monthly means (1980–1999) from the observational analysis of Behringer et al. (1998); crosses indicate the monthly climatology over this period. Solid line is the model parameterization, which is calibrated to the dots.

Note that the slope of the parameterization would be somewhat less steep if the fit were done to the climatology, since time-averaging of the ever-fluctuating thermocline tends to smooth out the vertical thermal profile. The smoothed climatological profile is the one more relevant to a simulation of climatological SST done with constant winds, since the missing time-mean effects of variability would be implicitly included in the parameterization. For simplicity, however, we shall use the sharper "instantaneous" profile for both the climatology simulation and the anomaly simulations. The steeper T_e parameterization will help to eliminate excessive cooling in the central Pacific where the simulated thermocline is slightly too shallow.

Fig. 4.8 shows a comparison of the model parameterization of T_e anomalies with the observed temperature anomalies at 50 m. The observed anomalies show little propagation except for some eastward propagation in the far eastern Pacific. The parameterized anomalies, on the other hand, show pronounced eastward propagation in the west/central equatorial Pacific, associated with the propagation of thermocline depth anomalies. Thus the parameterization is poorest in the central Pacific (180°W–140°W), where entrainment temperature anomalies are underestimated during ENSO events. This is likely the result of zonal advection below 50 m depth, which is ignored by the exclusive thermocline depth dependence of (4.22). In reality, eastward undercurrent anomalies act on the mean westward gradient of temperature to warm the subsurface in the central Pacific during El Niño, and westward undercurrent anomalies tend to cool the central Pacific during La Niña. In the intermediate model, part of this effect will be accounted for by advection in the mixed layer. However, we expect that the model will probably underestimate the SST variability in the central Pacific.

Many studies have shown that in the tropics and at interannual time scales, the net surface heat flux generally acts as a damper on SST anomalies (Liu and Gautier, 1990; Barnett et al., 1991; Cayan, 1992; Auad et al., 2001), except possibly in the central basin where evaporative changes associated with trade wind variability can sometimes enhance SSTAs (Seager, 1989). In the present model, we parameterize the surface heat flux as a linear restoring of the SST to a latitudinally-dependent temperature field $T_0(y)$, shown in Fig. 4.9 for the standard parameters of Table 4.2. For an SST damping rate of $\epsilon = 20$ W m^{-2} K^{-1}, this parameterization does a good job reproducing the observed surface heat flux, both for the climatology and the anomalies (Fig. 4.10). For the anomalies, the parameterization is better for the east Pacific than for the central Pacific. This is because changes in wind speed, which are not accounted for by the parameterization, induce substantial variability of the latent cooling over the central Pacific.

The entrainment efficiency γ and horizontal eddy diffusivity κ are chosen so that the mixed layer model reproduces observed SSTs when forced with observed wind stresses and entrainment temperatures. Fig. 4.11 shows that for the standard values of these parameters in Table 4.2, the model does a good job reconstructing the observed SST anomalies given the observed stress anomalies and T_e anomalies. There is a slight cold bias in the western Pacific and a slight warm bias near 120°W. The long-term warming trend evident in the NCEP ocean analysis is not reproduced in the intermediate model simulation, perhaps because the latter assumes no change in the radiative equilibrium temperature over the simulation period.

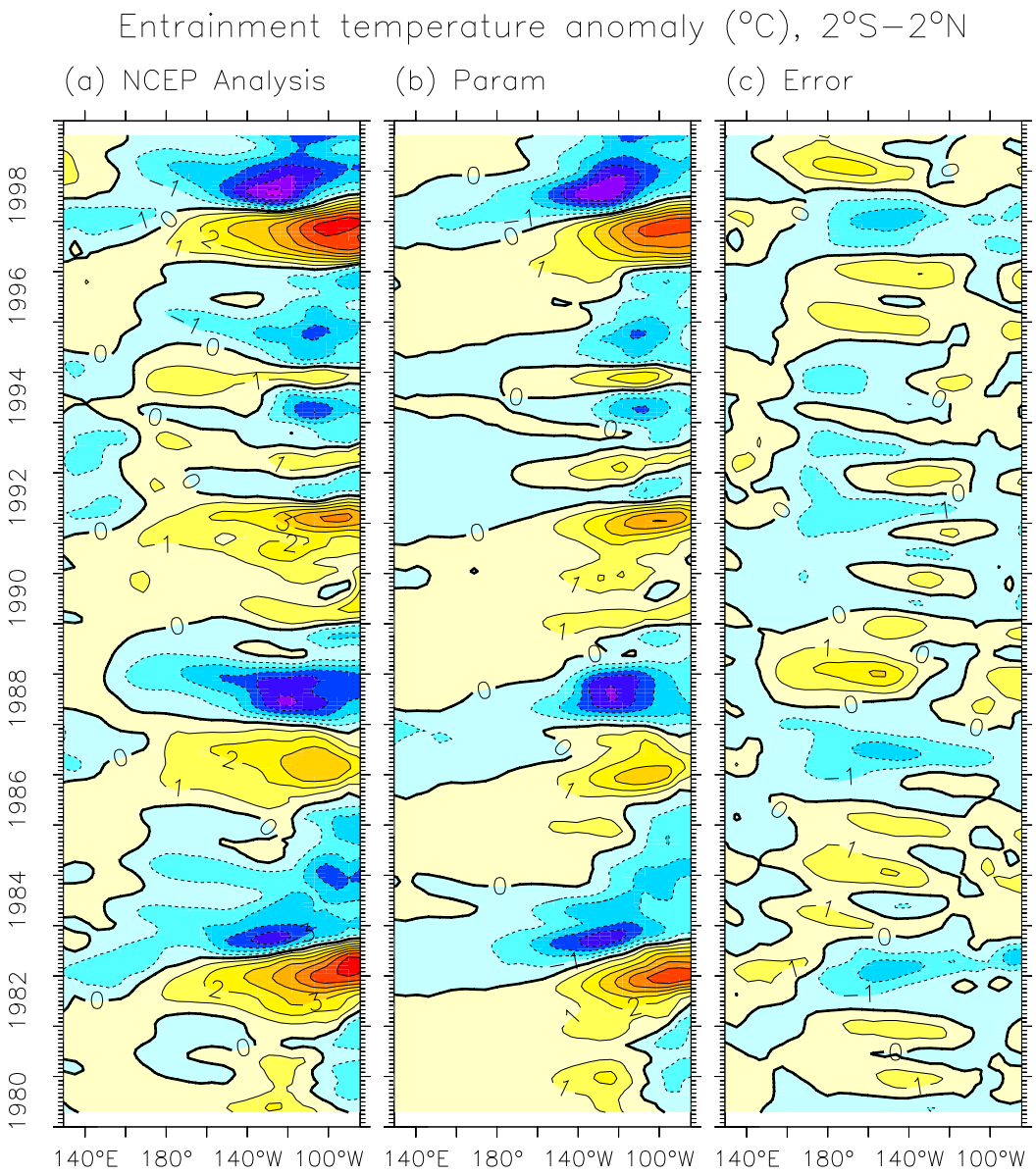

Figure 4.8: Anomalous temperature at 50 m depth, averaged over 2°S–2°N and smoothed with a 7-month triangle filter. (a) Observed anomalies from the analysis of Behringer et al. (1998). (b) Model parameterization in terms of the depth of the 20°C isotherm from Behringer et al. (1998). (c) Parameterization minus observations.

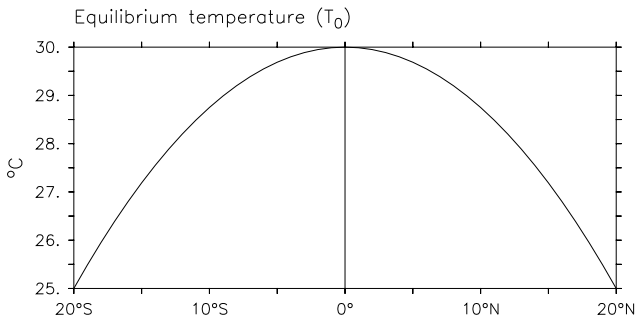

Figure 4.9: Meridional structure of the equilibrium temperature field $T_0(y)$, toward which SST is restored in the intermediate model.

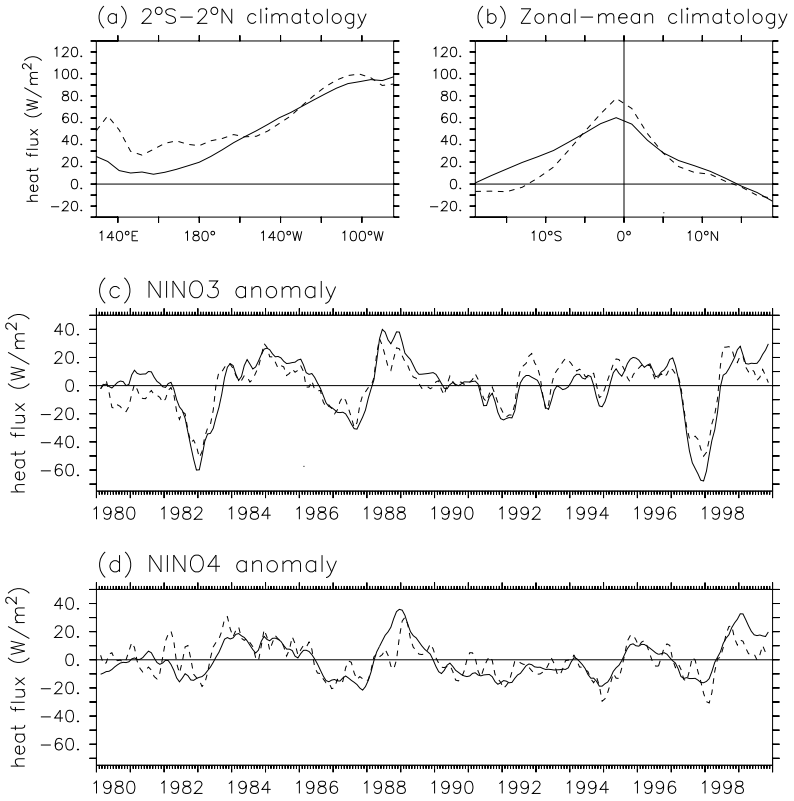

Figure 4.10: Dashed curves are the observed total surface heat fluxes into the ocean from the NCEP reanalysis (Kalnay et al., 1996) over the 1980–1999 period. Solid curves are the parameterized fluxes based on the reanalysis SST. Anomalies are with respect to the monthly climatology and have been smoothed with a 3-month triangle filter. (a) Time-mean heat flux averaged over 5°S–5°N. (b) Time-mean heat flux averaged zonally across the basin. (c) Anomalous heat flux averaged over the NINO3 region (150°W–90°W, 5°S–5°N). (d) Anomalous heat flux averaged over the NINO4 region (160°E–150°W, 5°S–5°N).

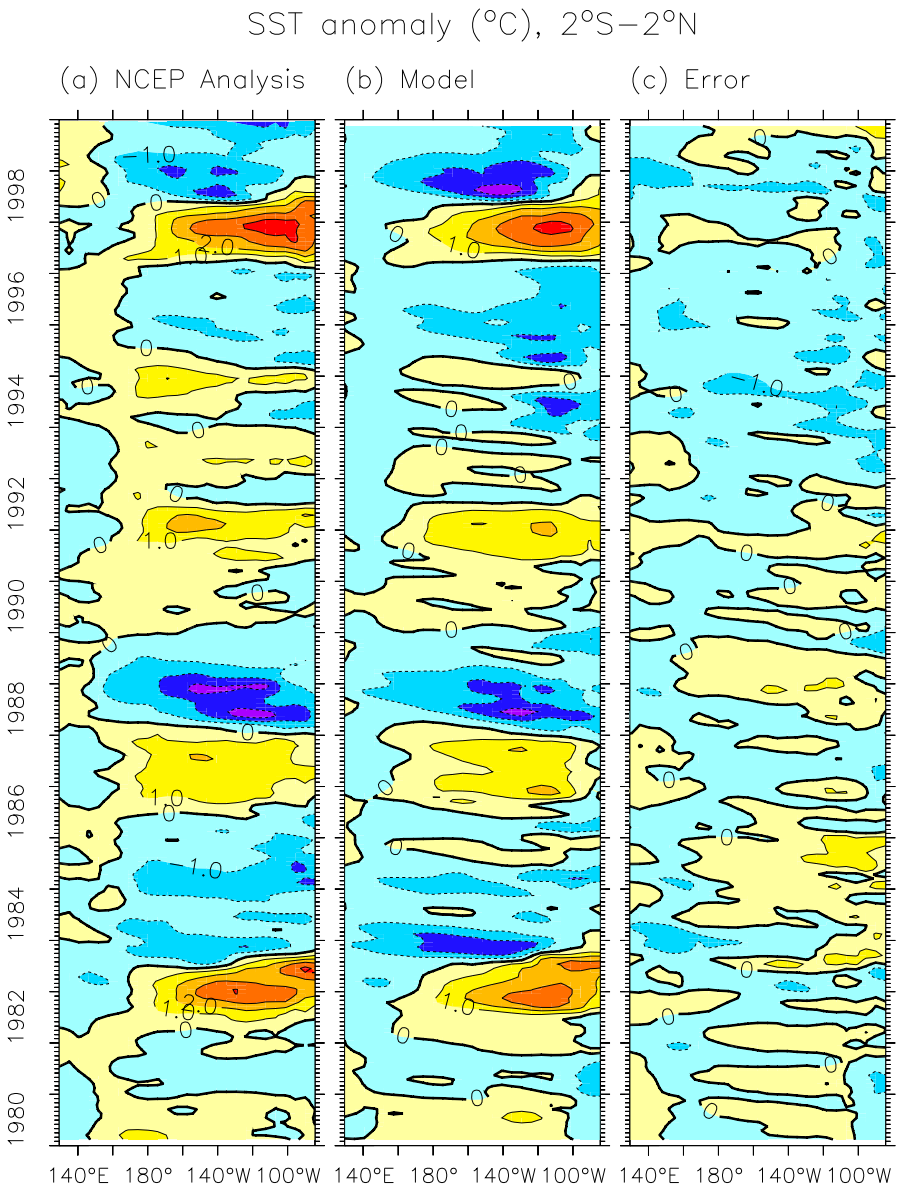

Figure 4.11: SST anomaly (°C), averaged over 2°S–2°N and smoothed with a 3-month triangle filter. (a) Observational analysis of Behringer et al. (1998). (b) Model forced with analyzed stress anomalies from FSU and analyzed 50 m temperature anomalies from Behringer et al. (1998). The climatological temperatures for the model are set equal to the 1980–1999 climatology from the Behringer et al. (1998) analysis, while the climatological currents are simulated by forcing with the FSU stress climatology for that period. (c) SST anomaly error, model minus observations.

4.2.4 Climatology simulation

Mean fields

To simulate the annual-mean climatology of the tropical Pacific ocean, the model is spun up for 10 years using the FSU stress climatology for the 1980–99 period. Fig. 4.12 shows that the model does a good job reproducing the observed thermal structure of the equatorial ocean, although the simulated SST is slightly too warm in the central Pacific. The simulated upwelling at the base of the mixed layer is slightly stronger than, and shifted east of, that in the Behringer et al. (1998) analysis. The simulated zonal current in the mixed layer is more strongly westward than the analyzed zonal current in the upper 50 m, because in the analysis the eastward undercurrent extends above 50 m depth in the eastern Pacific (i.e. in reality the mixed layer is shallower than 50 m in the east). The model also does a decent job simulating the zonal-mean climatological fields (Fig. 4.13). The off-equatorial errors in the subsurface thermal structure are of little concern, because there is very little upwelling in those regions to communicate such errors to the surface.

Climatological heat budget

A time-dependent variable ψ may be split into two components: a climatology (cyclic time-mean) $\overline{\psi}$ and an anomaly ψ' from this climatology: $\psi = \overline{\psi} + \psi'$. The climatology of (4.18) is

$$\begin{aligned} \partial_t \overline{T} \;=\; & -\overline{u}\partial_x \overline{T} - \overline{u'\partial_x T'} - \overline{v}\partial_y \overline{T} - \overline{v'\partial_y T'} \\ & -\overline{\mathcal{R}(w)}\,\partial_z \overline{T} - \overline{\mathcal{R}'(w)\partial_z T'} \\ & +\kappa\nabla^2 \overline{T} - \epsilon(\overline{T} - T_0) \end{aligned} \tag{4.25}$$

where $\mathcal{R}'(w) \equiv \mathcal{R}(w) - \overline{\mathcal{R}(w)}$. This equation describes the exact evolution of the climatological SST, assuming the completeness of (4.18).

The shallow-water model is linear and damped. Thus when the ocean model is forced with steady winds, it converges to a steady state climatology. In this case the climatological mixed layer heat balance is

$$\begin{aligned} \partial_t \overline{T}\big|_{model} &= 0 \\ &= -\overline{u}\partial_x \overline{T} - \overline{v}\partial_y \overline{T} - \mathcal{R}(\overline{w})\partial_z \overline{T} + \kappa\nabla^2 \overline{T} - \epsilon(\overline{T} - T_0) \end{aligned} \tag{4.26}$$

Note that the eddy terms of (4.25) are absent from (4.26), due to the lack of variability in the climatological wind stress forcing.

The annual-mean surface heat budget, neglecting temporal eddy terms, is shown in Fig. 4.14. The surface flux, which acts to restore the SST to T_0, is the largest single term in the heat budget. The existence of the equatorial cold tongue can be attributed to vertical entrainment, which dominates the heat budget in the east. Horizontal advection, which carries the cooling westward, becomes larger than the vertical entrainment term west of 140°W. Meridional advection carries cold water to the equator from the upwelling zone just south of the equator in the eastern Pacific; it also acts to widen the cold tongue by spreading it poleward. The horizontal mixing (eddy diffusion) also spreads the cold tongue,

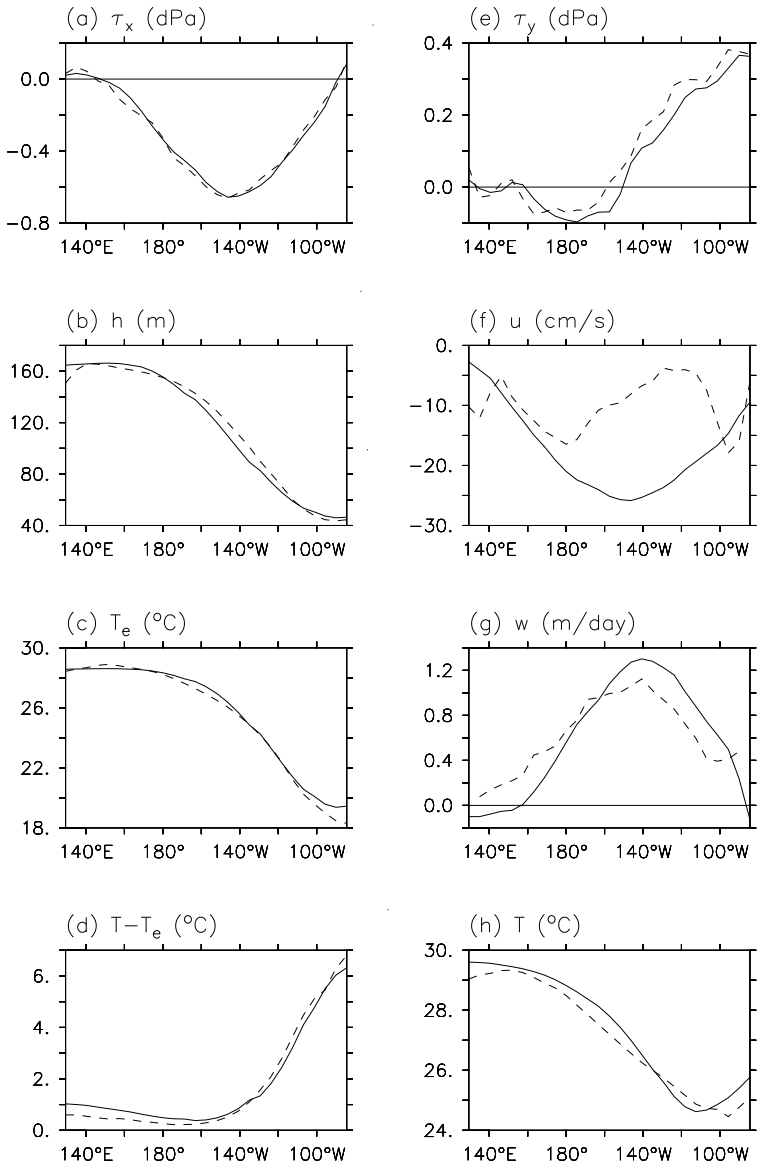

Figure 4.12: Annual-mean oceanic climatological fields at the equator (2°S–2°N). Dashed lines are from the observational analysis of Behringer et al. (1998). Solid lines are from the standard version of the intermediate model forced by the 1980–99 FSU stress climatology. (a) Zonal wind stress, (b) depth of the 20° isotherm, (c) temperature at 50 m, (d) temperature at surface minus that at 50 m, (e) meridional wind stress, (f) zonal current averaged over the top 50 m, (g) vertical velocity at 50 m, (h) SST.

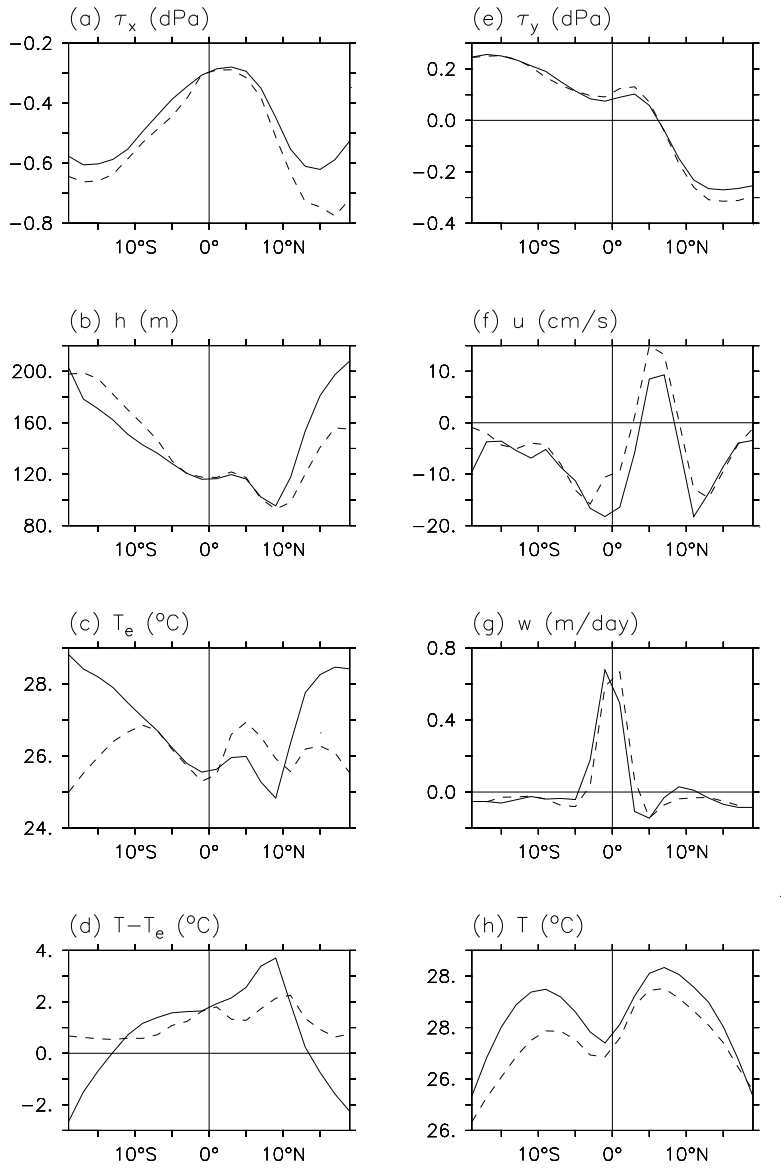

Figure 4.13: As in Fig. 4.12, but for zonal-mean fields.

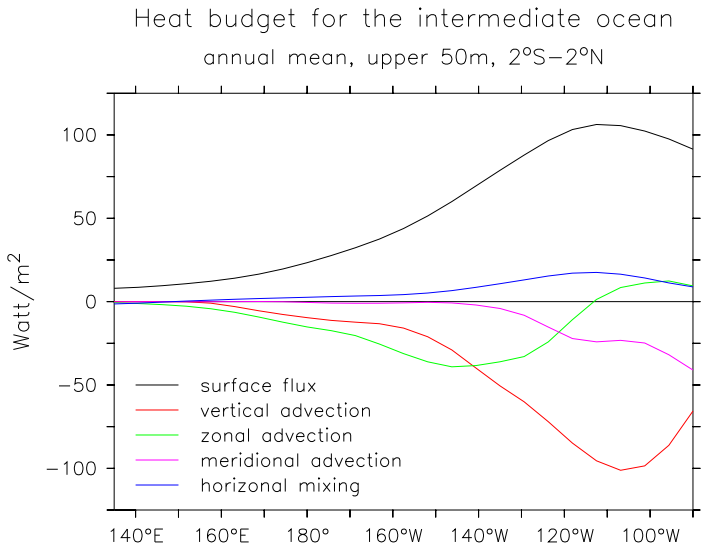

Figure 4.14: Annual-mean surface heat budget (Watts m^{-2}) in the standard model forced by the climatological FSU stresses from 1980–1999. Budget terms are averaged over the equatorial band (2°S–2°N); temporal eddy terms are neglected. Positive values indicate a warming effect on the mixed layer.

by exchanging cold water near the equator with warmer water away from it; mixing thereby acts as a weak damping on the equatorial SST anomalies.

Fig. 4.14 indicates that vertical entrainment will be the key to understanding SST variability in the eastern equatorial Pacific. The other terms in the heat budget are either smaller or act primarily to damp or spread the anomalies generated by entrainment. The longitudinal phase difference between entrainment and zonal advection also suggests that the interplay between these terms may determine whether SST anomalies propagate eastward or westward. This interplay, in turn, is keenly dependent on the structure of the mean state: entrainment dominates in the east because there the thermocline is shallow, and zonal advection dominates in the central Pacific because there the zonal gradient of SST is strong. Thus Fig. 4.14 provides much of the motivation and explanation for the results in this thesis.

4.2.5 ENSO simulation

Next, the climatological fields from Section 4.2.4 are used as the background state for a model simulation forced by observed stress anomalies for 1980–1999. The active layer depth H for the anomaly simulation is taken to be the average, zonally across the basin and meridionally across the 8°S–8°N latitude band, of the thermocline depth from the climatology simulation.

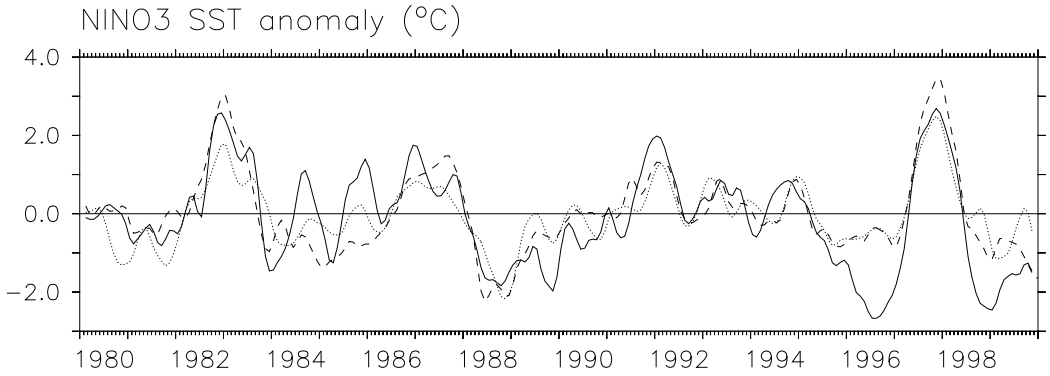

Figure 4.15: SST anomaly (°C) averaged over the NINO3 region (5°S–5°N, 150°W–90°W) and smoothed with a 3-month triangle filter. Dashed line is the observational analysis of Behringer et al. (1998). Solid line is the standard model forced by the FSU stress anomalies; dotted line is forced by the NCEP stress anomalies.

Importance of the stress forcing

Fig. 4.15 illustrates how forcing with different stress products can impact the simulation of SST anomalies. For both the FSU and NCEP stress products, the model underestimates the intensities of the 1984–86 cold period and the 1982–83 and 1997–98 warm events. However, beginning in 1984 the NCEP forcing generally produces NINO3-average SST anomalies with better timing and amplitude than does the FSU forcing. This is especially the case during 1984–87, 1996, and 1998–99. In particular, the NCEP forcing gives much weaker easterly stress anomalies than FSU during the late 1990s, which produces weaker (and more realistic) cold events during that period. Before 1984, however, the NCEP forcing produces somewhat less realistic-looking SST anomalies than does the FSU forcing (see Chapter 2).

Anomaly fields

A comparison between the observed and FSU-forced model SST anomalies at the equator for this period is shown in Fig. 4.16. The simulation looks reasonably similar to the observations, although the model anomalies are more confined to the eastern Pacific than observed. The model shows too much SSTA variance at periods less than one year, due to a similar problem with the thermocline simulation (Fig. 4.3). This could be due to limitations of the stress forcing (Chapter 2), perhaps amplified by the spurious basin resonance noted earlier. The simulated cold events in 1996 and 1998–1999 are too strong, perhaps again due to errors in the FSU stress forcing; and the simulation lacks the observed warming trend, possibly due to the model's neglect of temporal changes in the long-term radiative balance.

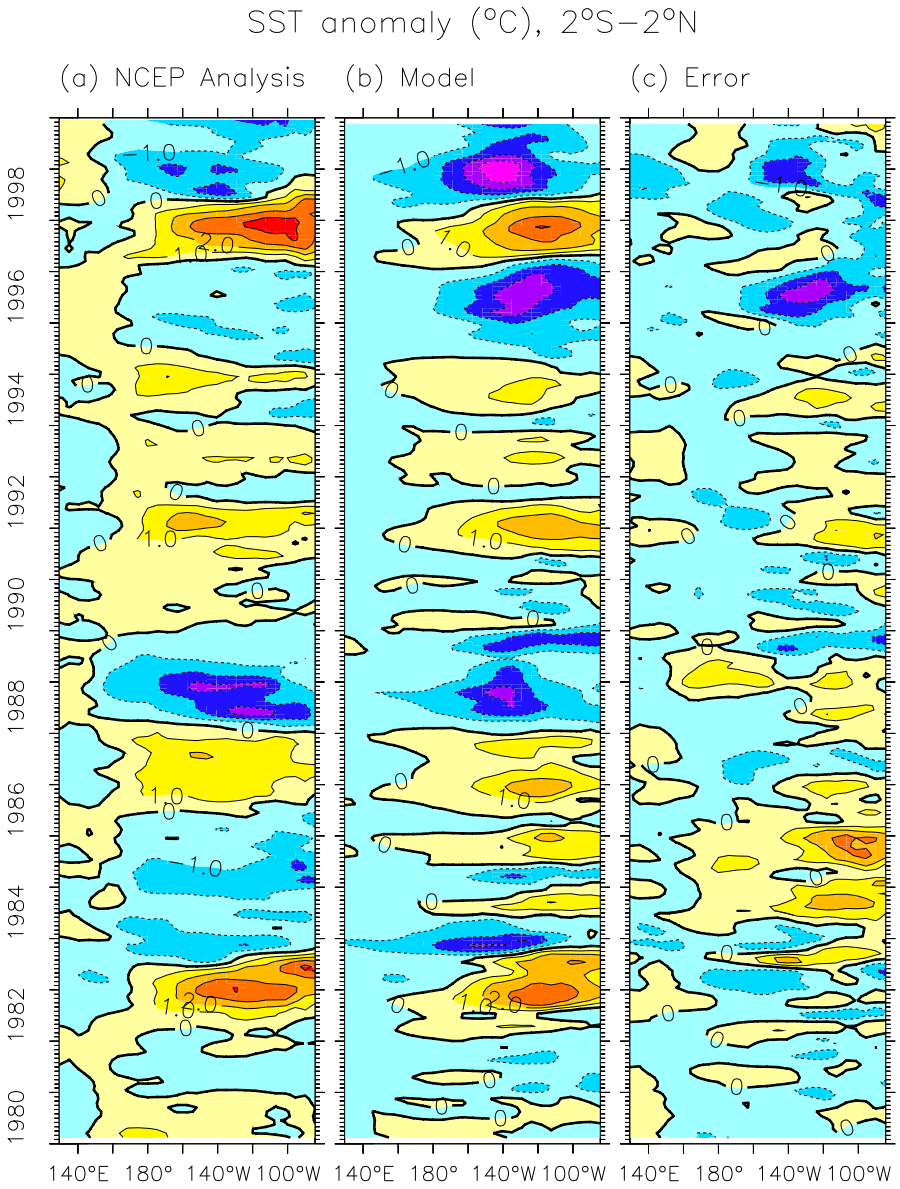

Figure 4.16: SST anomaly (°C) averaged over 2°S–2°N and smoothed with a 3-month triangle filter. (a) Observational analysis of Behringer et al. (1998). (b) Model forced with analyzed stress anomalies from FSU. The climatological background state for the model is simulated by forcing with the FSU stress climatology for that period. (c) SST anomaly error, model minus observations.

Anomalous heat budget

Subtracting (4.25) from (4.18) gives the exact SSTA tendency equation:

$$\begin{aligned}\partial_t T' \;=\; & -u'\partial_x\overline{T} - \overline{u}\partial_x T' - (u'\partial_x T')' \\ & -v'\partial_y\overline{T} - \overline{v}\partial_y T' - (v'\partial_y T')' \\ & -\mathcal{R}'(w)\partial_z\overline{T} - \gamma\overline{\mathcal{R}(w)}\partial_z T' - (\mathcal{R}'(w)\partial_z T')' \\ & +\kappa\nabla^2 T' - \epsilon T'\end{aligned} \tag{4.27}$$

The model SSTA tendency equation, on the other hand, is obtained by subtracting (4.26) from (4.18):

$$\begin{aligned}\partial_t T'\big|_{model} \;=\; & -u'\partial_x\overline{T} - \overline{u}\partial_x T' - u'\partial_x T' \\ & -v'\partial_y\overline{T} - \overline{v}\partial_y T' - v'\partial_y T' \\ & -\mathcal{R}^*(w)\partial_z\overline{T} - \mathcal{R}(\overline{w})\partial_z T' - \mathcal{R}^*(w)\partial_z T' \\ & +\kappa\nabla^2 T' - \epsilon T'\end{aligned} \tag{4.28}$$

where $\mathcal{R}^*(w) \equiv \mathcal{R}(w) - \mathcal{R}(\overline{w})$. The model SSTA tendency (4.28) differs from the exact SSTA tendency (4.27) because the model climatology neglects the effects of transient eddies (such as ENSO). As a result, anomalies simulated using (4.28) in a fully-coupled model may have nonzero mean.

If one were to assume, for the sake of contradiction, that the primed terms in (4.28) had zero mean, then the time average of (4.28) would be

$$0 = -\overline{u'\partial_x T'} - \overline{v'\partial_y T'} - \overline{\mathcal{R}^*(w)\partial_z T} \tag{4.29}$$

where the last term contains the total $\partial_z T$ due to the nonlinearity of the ramp function. Thus there will be no climate drift if the anomalous currents and temperature gradients are temporally uncorrelated and the total upwelling never changes sign. If the terms on the RHS of (4.29) are large and do not cancel, then the anomalies will develop nonzero mean values, which will then feed back on the climatology through the linear terms in (4.28) as well as through the nonlinear terms. The net effect of the eddy terms on the time mean of (4.28) will provide a measure of their possible role in the observed climatology.

Figs. 4.17 and 4.18 show the anomalous heat budgets at the surface in the eastern and western equatorial Pacific, respectively, for the simulation forced by observed stresses and entrainment temperatures (Fig. 4.11). The anomalous heat budget largely mirrors the climatological heat budget (Fig. 4.14). At 110°W, SST anomalies are generated primarily by mean upwelling acting on the anomalous vertical temperature gradient ($-\mathcal{R}(\overline{w})\partial_z T'$), with a contribution also from anomalous upwelling ($-\mathcal{R}^*(w)\partial_z\overline{T}$). Nonlinear and horizontal advection terms are generally small at 110°W, except during 1982 when anomalous eastward currents make a substantial contribution to the generation of a large warm event.

In contrast, at 170°W the zonal advection terms dominate the heat budget. Here the $-u'\partial_x\overline{T}$ and $-\overline{u}\partial_x T'$ terms act in concert to generate SST anomalies, while the nonlinear term $-u'\partial_x T'$ strongly opposes the generation of anomalies during warm events when the zonal gradient of total SST nearly vanishes. The complexity and nonlinearity of the heat

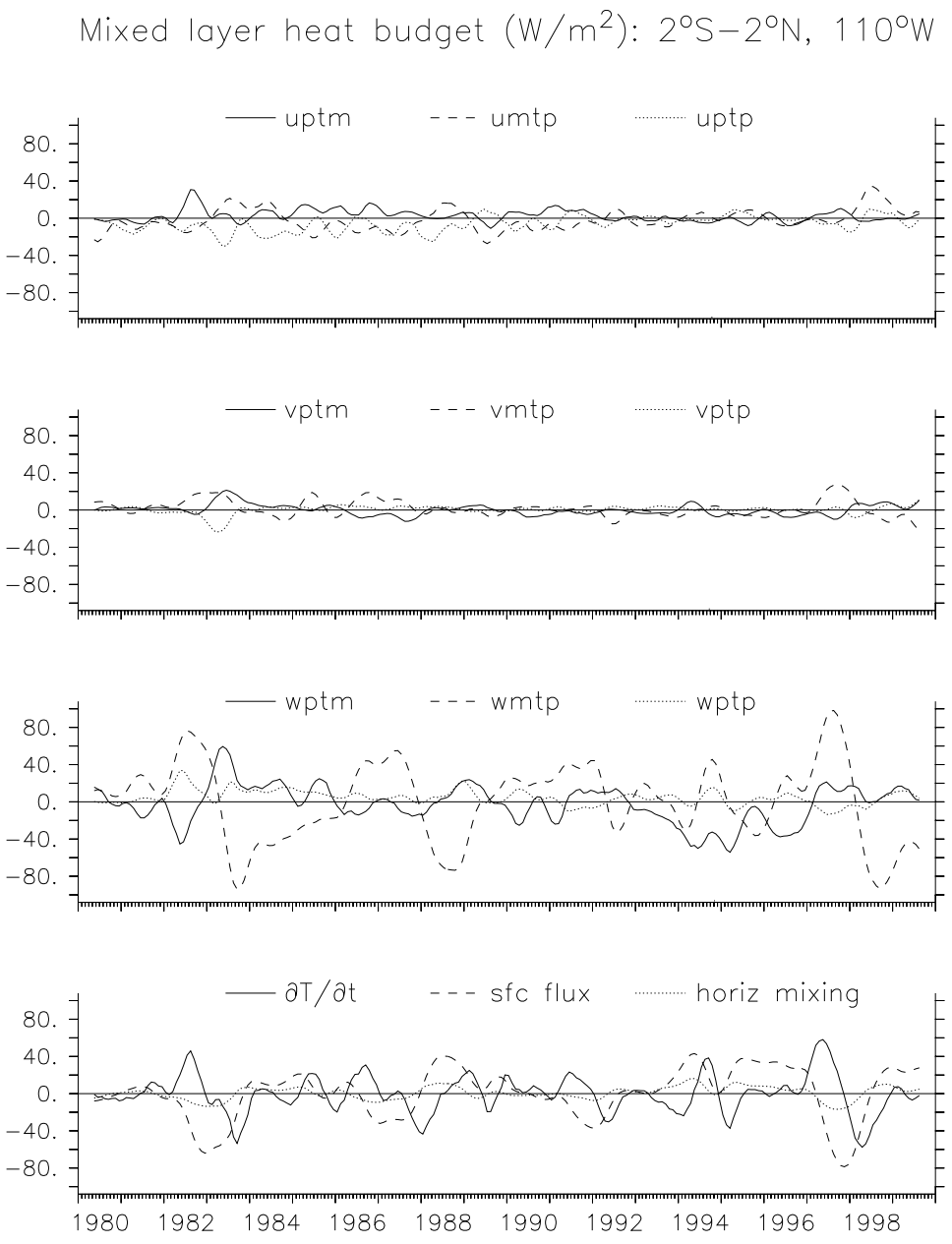

Figure 4.17: Mixed layer temperature tendency terms (Watts m^{-2}) at 110°W for the stress-forced simulation of Fig. 4.16, averaged over 2°S–2°N and smoothed with a 9-month triangle filter.

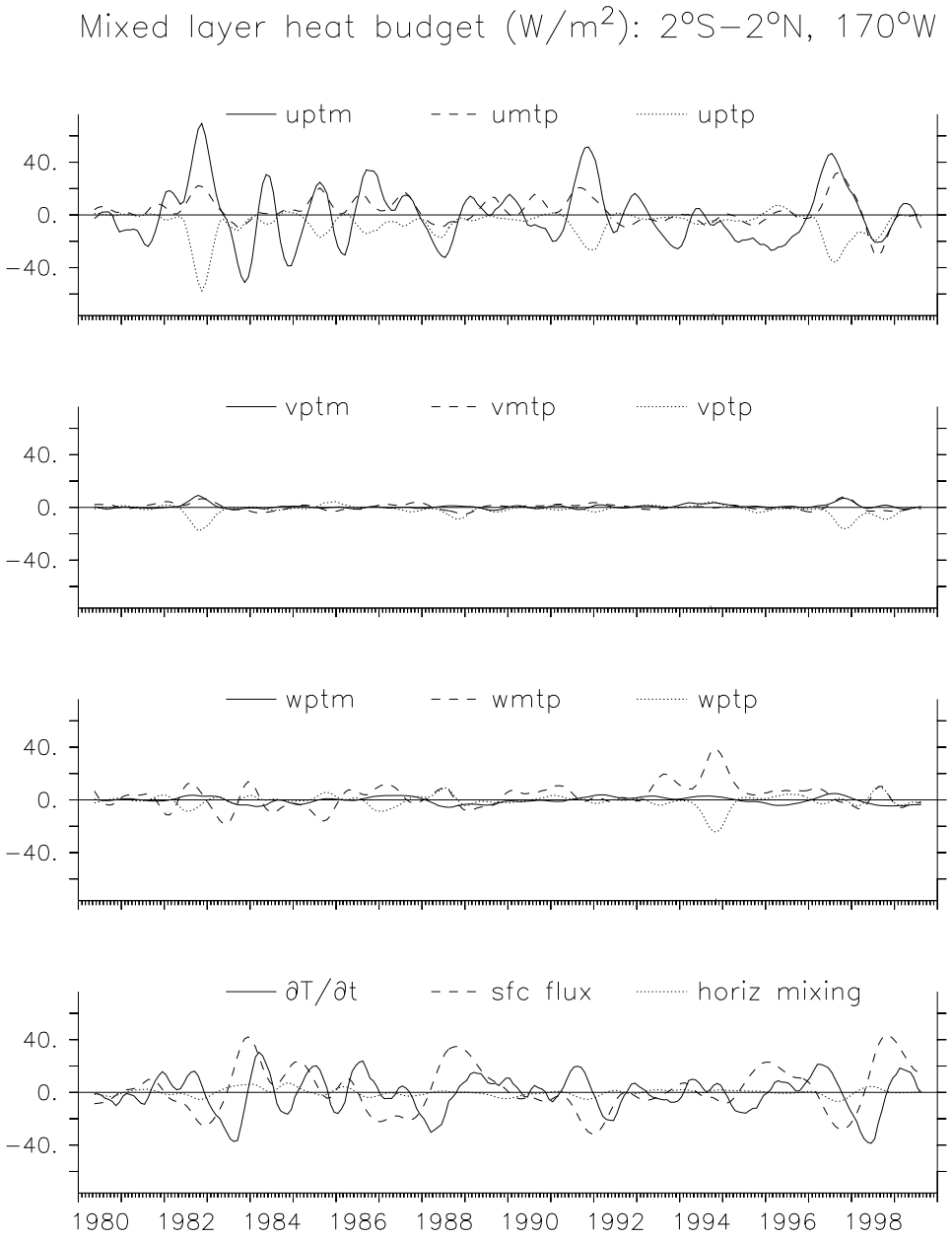

Figure 4.18: As in Fig. 4.17, but at 170°W.

Table 4.3: Stress perturbation parameters and their standard values.

Parameter	Symbol	Value
amplitude (weak)	$\tilde{\tau}_x^*$	0.001 dPa
amplitude (strong)	$\tilde{\tau}_x^*$	0.5 dPa
zonal position	x^*	165°W
meridional position	y^*	0°N
zonal halfwidth	Δx^*	40° lon
meridional halfwidth	Δy^*	10° lon
duration	Δt^*	3 months

budget in the west may be one reason the zonal propagation characteristics of ENSO seem to vary from event to event. Slow changes in the zonal gradient of SST through time may alter the delicate balance of zonal advective terms, changing the temporal phasing of the SST peak in the west relative to that in the east, thereby affecting the zonal propagation characteristics of SST anomalies during ENSO events.

4.3 Coupled model

4.3.1 Control run

Experimental setup

Next, the statistical atmosphere from FSU (1980–1999) is coupled to the dynamical ocean model to produce a hybrid coupled anomaly model (see Appendix D for a caveat regarding anomaly models). The climatology is generated as in Section 4.2.4, except that it is now averaged over the calendar year to produce a time-invariant background state. The anomaly model is then subjected to a transient zonal stress anomaly in the western Pacific, with the form

$$\tau_x^* = \tilde{\tau}_x^* \left[\mathcal{S}(t) - \mathcal{S}(t - \Delta t^*)\right] \exp\left[- \left| \frac{x - x^*}{\Delta x^*} \right|^2 - \left| \frac{y - y^*}{\Delta y^*} \right|^2 \right] \tag{4.30}$$

where $\mathcal{S}$ is the Heaviside step function

$$\mathcal{S}(t) \equiv \begin{cases} 0 & : \quad t \leq 0 \\ 1 & : \quad t > 0 \end{cases} \tag{4.31}$$

Standard parameters for the stress perturbation are given in Table 4.3.

Response to a westerly wind event

Fig. 4.19 shows the response of the hybrid coupled model to a strong transient westerly stress anomaly ($\tilde{\tau}_x^* = 0.5$ dPa). The model responds with a strong initial warm event, followed by a regular oscillation with a 3.1 yr period and an e-folding decay timescale of about 10 yr. To first order, the SST anomalies, zonal stress anomalies, and thermocline depth anomalies are best described as developing in place and in phase. The SST anomalies

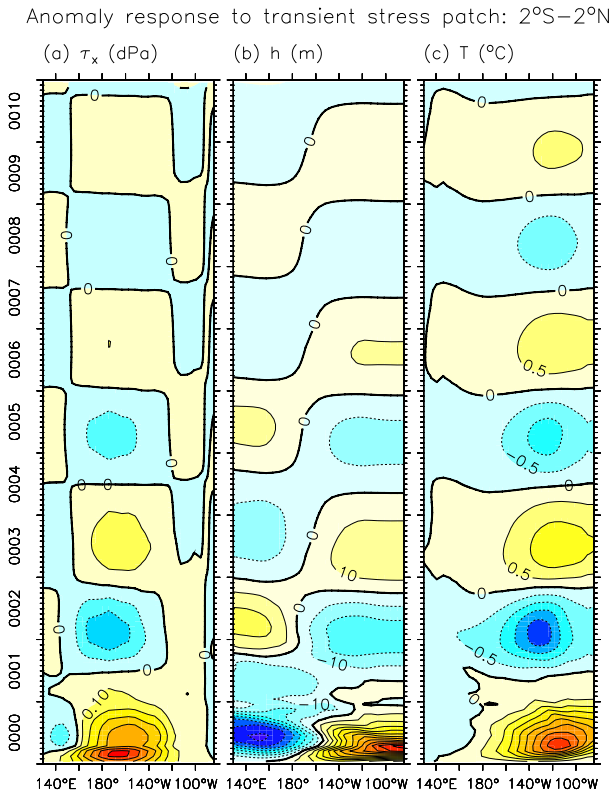

Figure 4.19: Equatorial (2°S–2°N) response of the standard hybrid coupled model to a transient westerly stress perturbation in the central Pacific: (a) zonal stress anomaly (dPa), (b) thermocline depth anomaly (m), (c) SST anomaly (°C). The amplitude of the initial stress perturbation is $\tilde{\tau}_x^* = 0.5$ dPa.

are focused near 120°W during warm events, slightly further west during cold events. The weak SST anomalies west of the dateline show evidence of westward propagation, and there is a slight hint of eastward propagation east of the dateline. The zonal stress shows peak westerly anomalies near 165°W during warm events, and peak easterly anomalies slightly further west during cold events. The thermocline exhibits an east-west seesaw about 170°W, deepening in the east and shoaling in the west during warm events. The thermocline depth near 170°W leads that in the eastern Pacific by a quarter cycle, giving the appearance of eastward propagation of the thermocline depth anomalies between events.

Figs. 4.20 and 4.21 show the heat budget of the mixed layer, starting in year 100 when the oscillation amplitude is significantly reduced and only the least damped mode remains. In this regime, the contributions of the nonlinear terms and $-v'\partial_y\overline{T}$ to the SST budget are small and can be ignored. As noted by Kang et al. (2001), the phase lag between each tendency term and the SSTA reveals the extent to which that term is an instability mechanism which acts to amplify ENSO, or a transitioning mechanism that acts to carry ENSO between warm and cold events. Fig. 4.20 indicates that the surface flux, for example, is a purely stabilizing mechanism in the present model since it is simply a linear damping

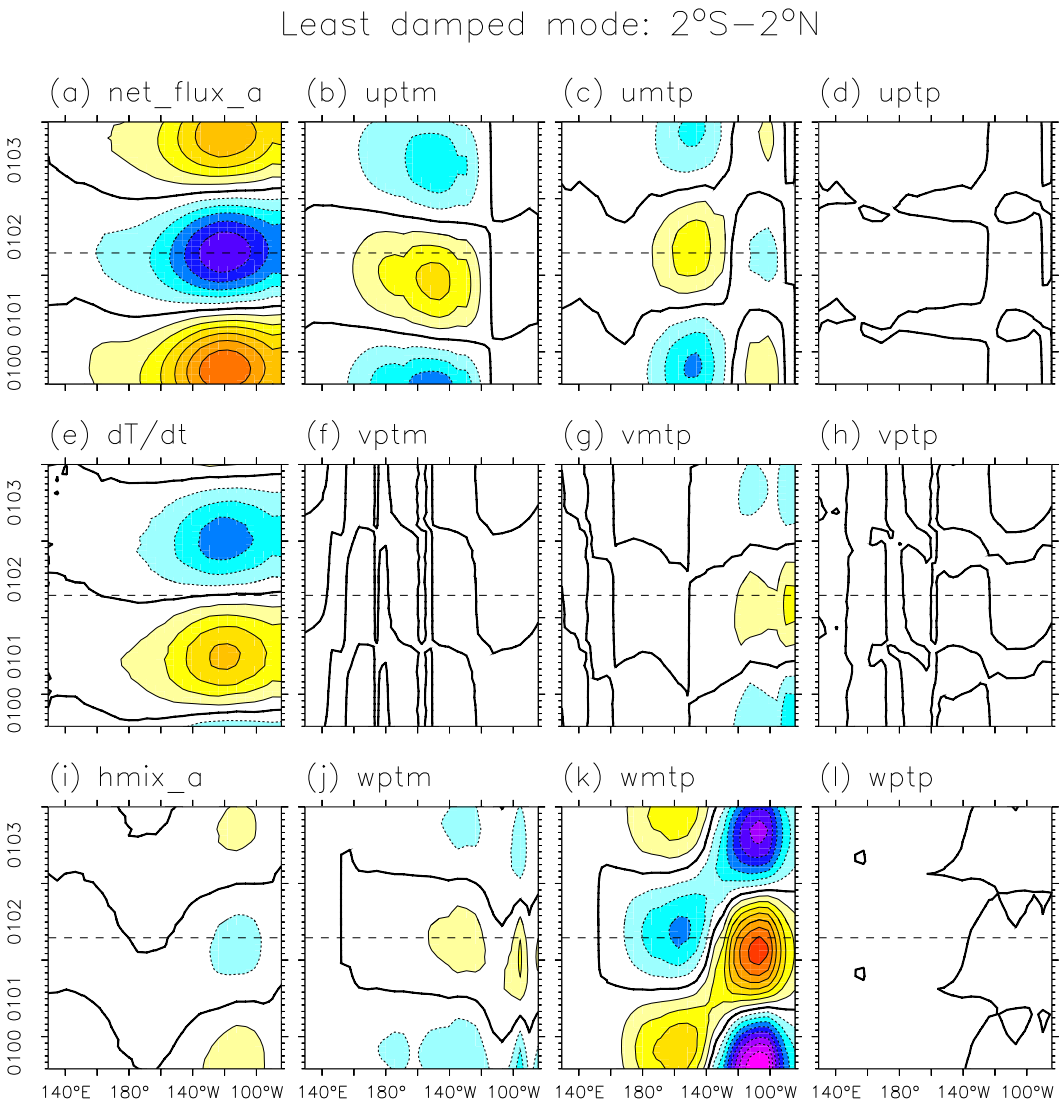

Figure 4.20: Mixed layer temperature tendency terms (averaged 2°S–2°N) for the experiment of Fig. 4.19, long after the initial perturbation when the oscillation is extremely weak and the dynamics are linear. Vertical axis indicates years since perturbation; dashed horizontal line indicates the peak of a warm event. Contour interval is 0.00025 Watts m^{-2}, heavy contour indicates zero; warm colors indicate positive values, cool colors negative values; near-zero values are not shaded. Panels show (a) $-\epsilon T'$, (b) $-u'\partial_x \overline{T}$, (c) $-\overline{u}\partial_x T'$, (d) $-u'\partial_x T'$, (e) $\partial_t T'$, (f) $-v'\partial_y \overline{T}$, (g) $-\overline{v}\partial_y T'$, (h) $-v'\partial_y T'$, (i) $\kappa\nabla^2 T'$, (j) $-\mathcal{R}^*(w)\partial_z \overline{T}$, (k) $-\mathcal{R}(\overline{w})\partial_z T'$, (l) $-\mathcal{R}^*(w)\partial_z T'$. SST anomaly is obtained by dividing the surface flux anomaly in (a) by $-\epsilon$.

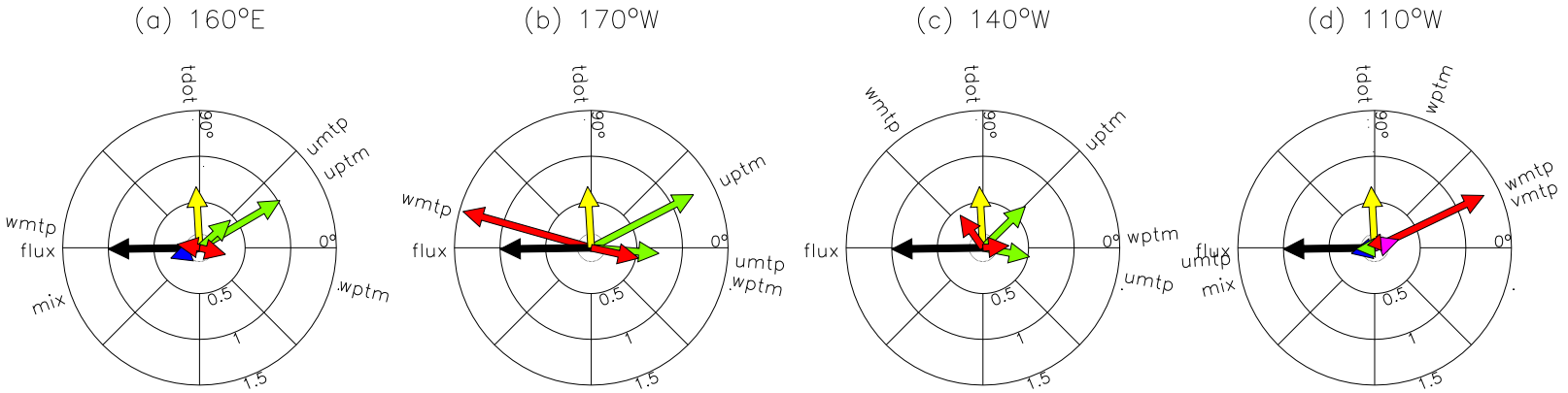

Figure 4.21: Mixed layer temperature tendency phasors (averaged 2°S–2°N) for the experiment of Fig. 4.19, long after the initial perturbation, at longitude (a) 160°E, (b) 170°W, (c) 140°W, (d) 110°W. Each diagram indicates the amplitude (relative to the surface heat flux) and phase lead (relative to local SSTA) of the tendency terms, and reads like a clock: a given phasor leads the one to its right. The peak SST warm anomaly occurs at 0° phase (3 o'clock). The graticule scale is labeled in units of the surface flux damping rate ϵ.

on SSTA.

The $-\mathcal{R}(\overline{w})\partial_z T'$ term plays important but varying roles all across the equatorial Pacific. In the eastern Pacific, $-\mathcal{R}(\overline{w})\partial_z T'$ leads SSTA slightly and therefore plays dual roles as an instability and transition mechanism. In the western/central Pacific, $-\mathcal{R}(\overline{w})\partial_z T'$ is almost perfectly out of phase with SSTA and so acts as a stabilizing mechanism. This is because in the western Pacific the model shows hardly any entrainment temperature anomalies; the vertical temperature gradient therefore follows the surface temperature and SSTAs are damped through mean upwelling.

Zonal advection plays an important role in the central and western Pacific. The $-u'\partial_x\overline{T}$ term, which is most active near 140°W, leads SSTA slightly more than $-\mathcal{R}(\overline{w})\partial_z T'$ and therefore plays a stronger role as a transitioning mechanism for the simulated ENSO. The transitioning role of $-u'\partial_x\overline{T}$ has been a common theme in recent studies. Picaut and Delcroix (1995) and Picaut et al. (1997), in particular, argued for its importance to the observed ENSO, proposing an advective-reflective conceptual model that depended strongly on zonal advection by Rossby signals reflected from the eastern boundary. The surface current anomalies are also important for redistributing mass within the tropical Pacific Ocean. Goddard and Philander (2000) examined the oceanic energy budget in a wind-forced ocean GCM, and found that the power input to the ocean by the mean wind stress acting on the anomalous currents, which preceded the peak SST anomalies by 3 months, was the greatest generator of available potential energy in the Pacific Ocean at interannual timescales.

The $-\overline{u}\partial_x T'$ term, on the other hand, acts as an SSTA amplifier in the central Pacific (on the western side of the SST anomalies generated by $-\mathcal{R}(\overline{w})\partial_z T'$), and a damper in the eastern Pacific (on the eastern side of the SST anomalies generated by $-\mathcal{R}(\overline{w})\partial_z T'$). Other terms play secondary roles; $-\overline{v}\partial_y T'$ and $-\mathcal{R}^*(w)\partial_z\overline{T}$ act to destabilize ENSO, while $\kappa\nabla^2 T'$ plays more of a stabilizing and "anti-transitioning" role. It is interesting to note that in the western basin, $-\mathcal{R}^*(w)\partial_z\overline{T}$ practically cancels the damping effect of $-\mathcal{R}(\overline{w})\partial_z T'$, so that zonal advection almost entirely controls the evolution of SST anomalies in this region.

The heat budget is somewhat different during the transient phase immediately following the stress perturbation. Fig. 4.22 shows the heat budget of the mixed layer during the first few years after the westerly wind event. Compared to the small-amplitude oscillation in Fig. 4.20, the transient behavior indicates a much stronger role for zonal advection and nonlinearity. The stress perturbation induces strong eastward current anomalies, which act to warm the central Pacific by advecting the warm pool eastward (Fig. 4.22b). As the east Pacific warms, the zonal SST gradient weakens and the effect of $-u'\partial_x\overline{T}$ is strongly opposed by $-u'\partial_x T'$. Vertical advection also contributes strongly to the initial warming in the east Pacific, as less water and warmer water is entrained into the mixed layer. The strong reduction in entrainment also implies a role for $-\mathcal{R}^*(w)\partial_z T'$, which reduces the impact of sub-mixed-layer temperature changes on SST. The warm event peaks soon after the imposed westerly stress is removed, as cold water is conveyed westward by Rossby waves reflected from the eastern boundary, and as the equatorial thermocline continues to shoal due to the strong off-equatorial wind stress curl associated with the atmospheric response to the SST warming. By 18 months the SST has returned to normal, but there is still a cooling tendency due to $-\mathcal{R}(\overline{w})\partial_z T'$ associated with the anomalously shallow equatorial

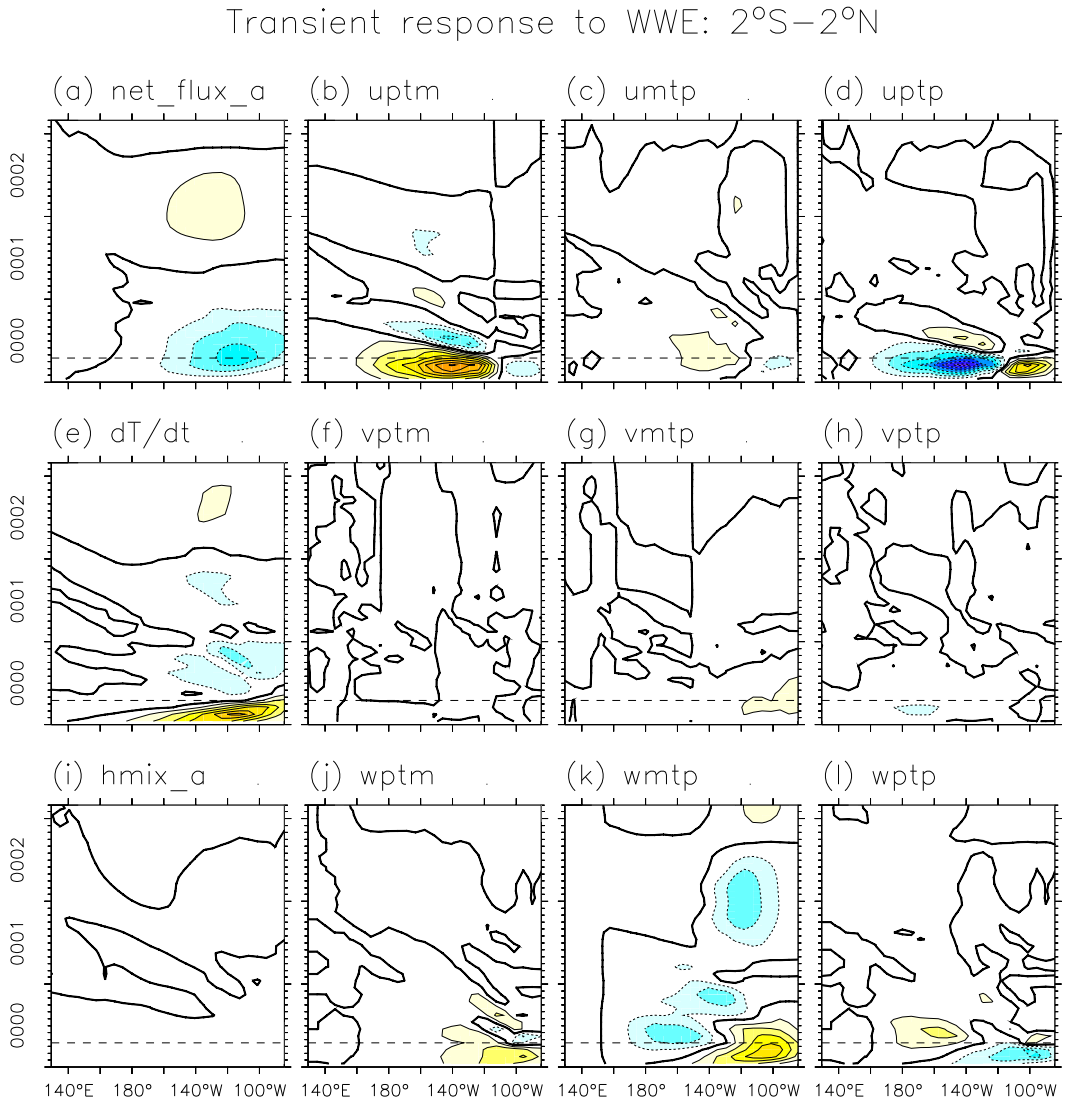

Figure 4.22: As in Fig. 4.20, but for the years during and immediately after the imposition of a strong westerly stress perturbation. Contour interval is 25 Watts m^{-2}.

thermocline. This cooling carries the system into a weak cold event, and the system settles into the modal behavior shown in Fig. 4.20.

Response to an easterly wind event

Fig. 4.23 shows the response of the model to an easterly stress perturbation ($\tilde{\tau}_x^* = -0.5$ dPa). Clearly, this response is not simply the opposite of that for a westerly wind event. The initial cooling develops rapidly in the central Pacific, due mostly to zonal advection. In contrast with Fig. 4.22, the nonlinear terms $-u'\partial_x T'$ and $-\mathcal{R}^*(w)\partial_z T'$ now act to *enhance* the initial effects of $-u'\partial_x \overline{T}$ and $-\mathcal{R}(\overline{w})\partial_z T'$, as anomalously strong currents act on an anomalously strong cold tongue. The cold event meets an abrupt end, as westerly anomalies develop in the east and cut off the source of cold water from the deep.

Thus we see that there is a fundamental difference in the way simulated strong warm and cold events develop and terminate. Warm events develop in the east via changes in vertical advection, especially that associated with vertical motions of the thermocline; zonal advection plays a secondary role during warm events since the zonal SST gradients are weakened. Cold events develop in the central Pacific via zonal advection, since the zonal SST gradients are enhanced during cold events; vertical advection plays a secondary role during cold events since the temperature of entrained water in the east can get no colder than the saturation temperature below the thermocline.

The simulated warm events, which are associated with westerly stress all along the equator, terminate because the off-equatorial cyclonic wind curl produces geostrophic divergence near the equator. This slowly drains warm water from the equatorial band, shoals the thermocline, and thereby reverses the SST tendency due to vertical advection. Cold events, which are associated with westerly stress near the dateline and easterly stress in the east, terminate due to zonal advection (associated with wave reflection at the eastern boundary, amplified by westerly stress anomalies in the east), and vertical advection (associated with the reduction of upwelling due to the westerly stress anomalies in the east)

4.3.2 Parameter sensitivity of the anomaly model

Before embarking on the climate sensitivity studies in the next chapter, we first investigate the sensitivity of the anomaly model to changes in its dynamical parameters. In these experiments, the background state is held fixed at the standard climatology described in Section 4.2.4. To connect with previous studies, we here introduce a "coupling parameter" μ which multiplies the stress anomalies produced by the statistical atmosphere. We take $\mu = 1.0$ as our standard value. Other important parameters include the active layer coefficients λ_h and λ_u, and the boundary reflectivities R_e and R_w.

Experimental setup

Two regimes are of interest. The first is the small-amplitude regime, where nonlinearities are weak and can be neglected. In this regime, after transient motions have decayed away, oscillations will take the form of a complex exponential that corresponds to the most unstable (or least damped) normal mode of the system. Often, the periods and growth

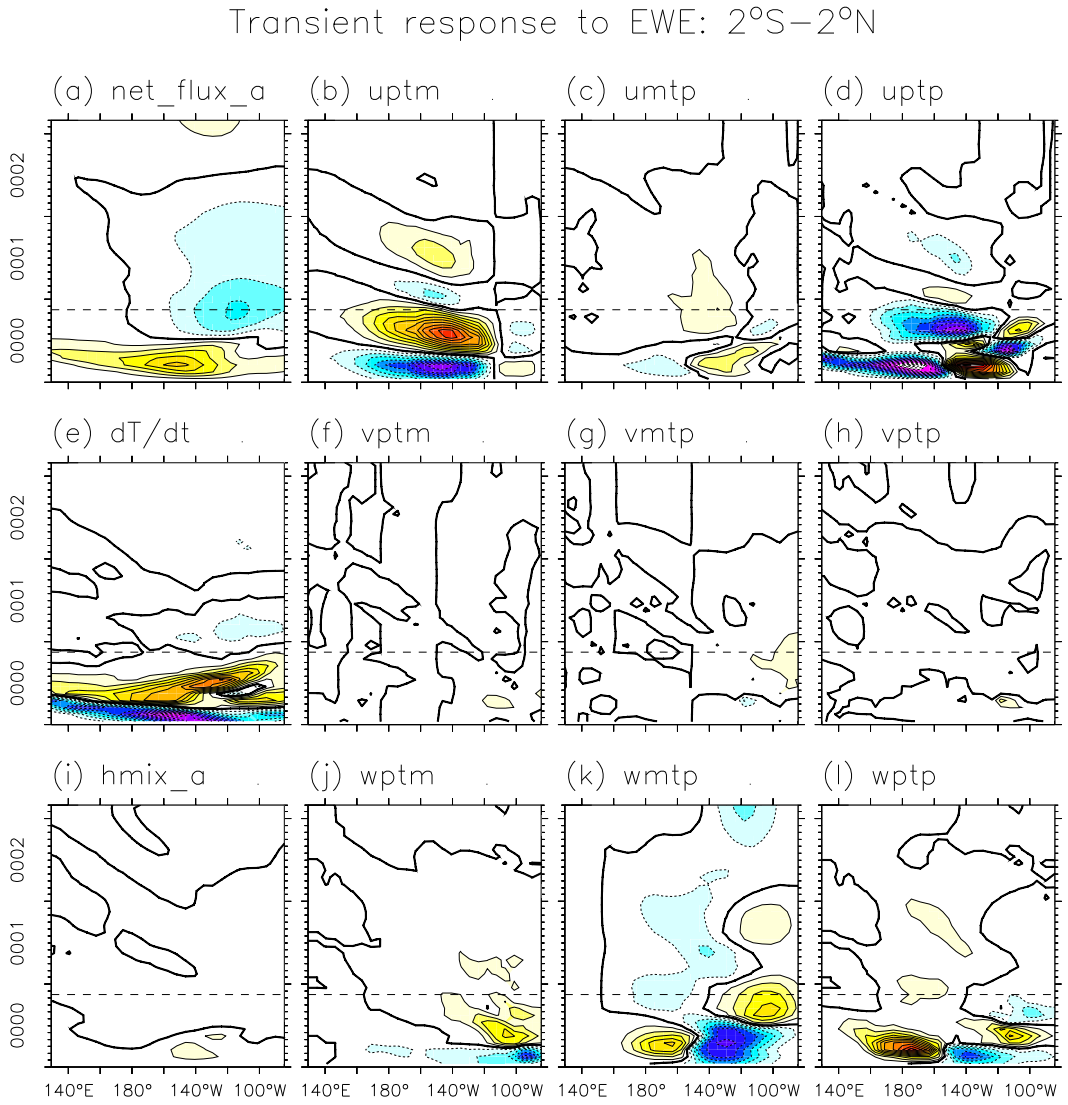

Figure 4.23: As in Fig. 4.22, but for the years during and immediately after the imposition of a strong easterly stress perturbation.

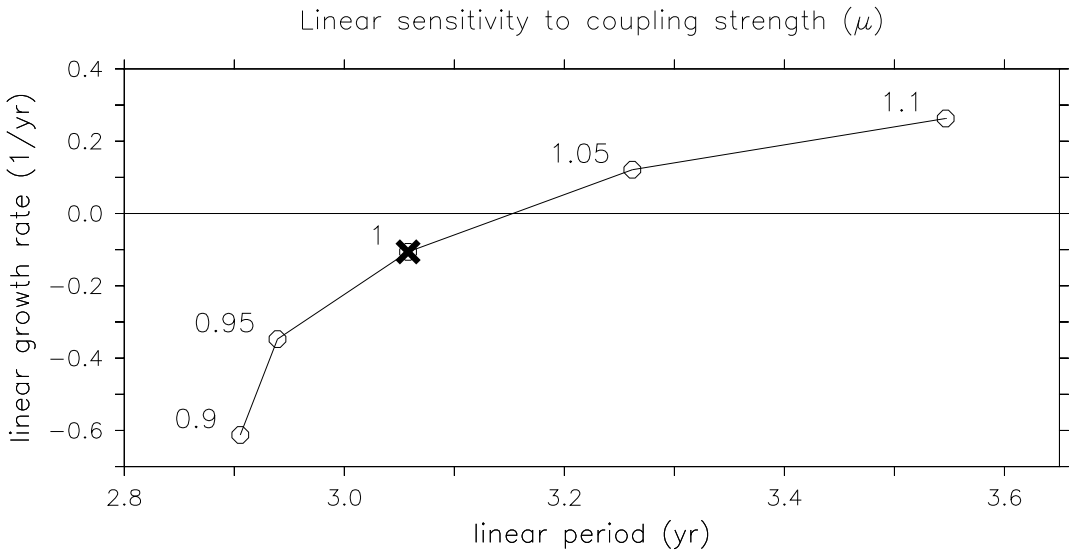

Figure 4.24: Dependence of the model linear growth rate (1/yr) and period (yr) on μ, the strength of the wind stress response to SST anomalies. Values of μ at the open circles are labeled. Standard model corresponds to $\mu = 1.0$ (X).

rates of the normal modes are obtained by casting the system in matrix form and solving the associated eigenproblem. In the present study, we estimate the period by counting the zero-crossings of the timeseries, and then estimate the growth rate by fitting exponential curves to and extrema of the timeseries. For small-amplitude oscillations this technique can recover the period and growth rate of the least damped mode, as long as the growth rate and nonlinear trend are small relative to the frequency. This technique is applied to the present model by perturbing with a very weak stress anomaly ($\tilde{\tau}_x^* = 0.001$ dPa), and then extracting the period and growth rate from the resulting timeseries of NINO3 SSTA.

The second regime of interest is the asymptotic regime, which is reached by the system long after the initial perturbation. The system may reach a stable fixed point, a stable limit cycle, or a strange attractor. Nonlinearity may be important in this regime and the oscillation may be absent or non-sinusoidal. To reach this regime, we perturb the model with a moderate stress anomaly ($\tilde{\tau}_x^* = 0.1$ dPa) and spin up the model for 100 yr. We then extract the time-mean, minimum, maximum, and oscillation period from the subsequent timeseries of NINO3 SSTA.

Sensitivity to air-sea coupling

Fig. 4.24 shows the sensitivity of the linear growth rate and period of the model ENSO to changes in μ, the strength of the wind stress response to SST anomalies. With increasing coupling, both the period and growth rate of the model ENSO increase. The standard coupling $\mu = 1.0$ is just below the neutral stability point. Note that the effect of coupling on the linear period is relatively minor: as μ increases from 0.9 to 1.1, the period goes from 2.9 yr to just under 3.6 yr.

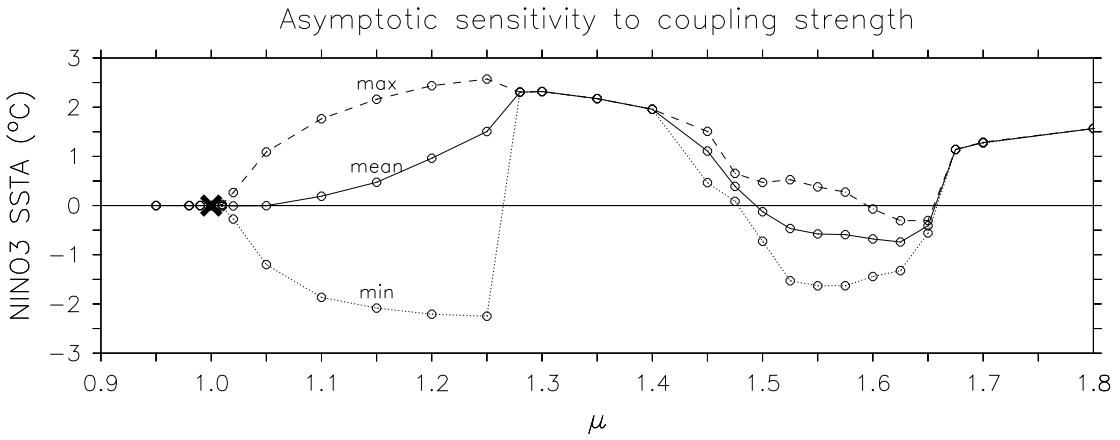

Figure 4.25: Dependence of model asymptotic behavior on μ, the strength of the wind stress response to SST anomalies. For each value of μ, the model is perturbed and then spun up for 100 yr. The minimum, maximum, and time-mean of a subsequent 50 yr timeseries of NINO3 SSTA are then plotted to give an indication of the amplitude and skewness of the model oscillation. The standard model ($\mu = 1.0$) is marked with an X.

The asymptotic sensitivity to coupling strength is shown in Fig. 4.25, for a wider range of μ. As the coupling increases, the system behavior shows several qualitative changes. Above the Hopf bifurcation near $\mu = 1.02$, the oscillation becomes more and more skewed, as warm events lengthen and cold events shorten. Around $\mu = 1.25$ the system plunges into a permanent El Niño. The oscillations appear once more above $\mu = 1.4$, as the model trajectory wanders a thicket of quasi-periodic orbits. Beyond $\mu = 1.65$, the system returns to a permanent El Niño.

Sensitivity to active layer coefficients

Fig. 4.26 shows the sensitivity of the linear growth rate and period to changes in the active layer coefficients. The growth rate increases with increasing λ_h and λ_u, just as it does with an increase in the air-sea coupling coefficient (Fig. 4.24). The period, however, increases with λ_h and decreases with λ_u. Thus along the neutral stability line of Fig. 4.26a, there is a change in the period of the least damped mode. At large λ_h and small λ_u, the mode is dominated by vertical advection, which imparts the slow time scale associated with equatorial recharge/discharge. At small λ_h and large λ_u, the mode is dominated by zonal advection, which introduces two fast time scales: one associated with wave reflection (which reverses the zonal current anomalies), and another associated with zonal propagation (which reverses the upwelling anomalies in the east by displacing the zonal stress anomalies). These two mode types were also evident in Figs. 4.22 and 4.23, except in that case the mode selection was achieved through nonlinearity rather than changes in model parameters. It is interesting to note that the model is most sensitive to the active layer coefficients in the zonal advective regime (small λ_h and large λ_u).

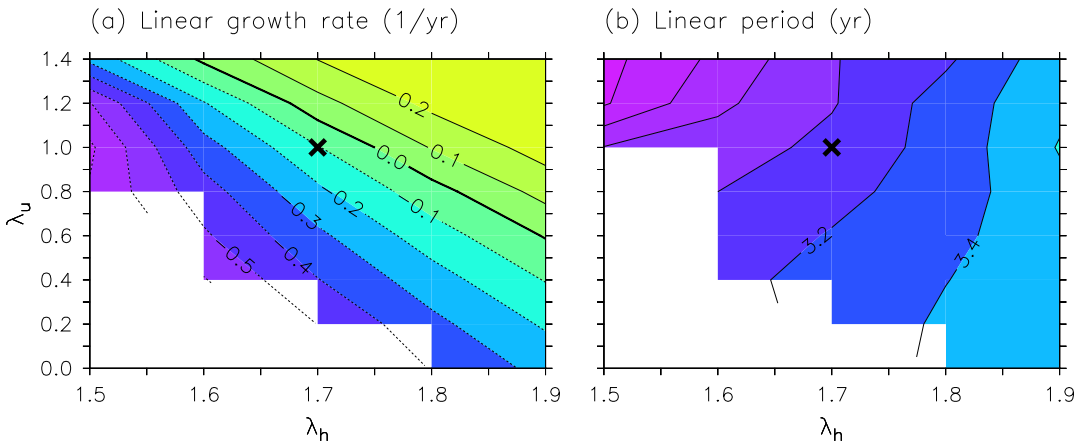

Figure 4.26: Dependence of (a) the linear growth rate (1/yr) and (b) the linear period (yr) on λ_h, the coefficient of active layer depth, and λ_u, the coefficient of active layer currents. Values for the standard model are indicated with an X.

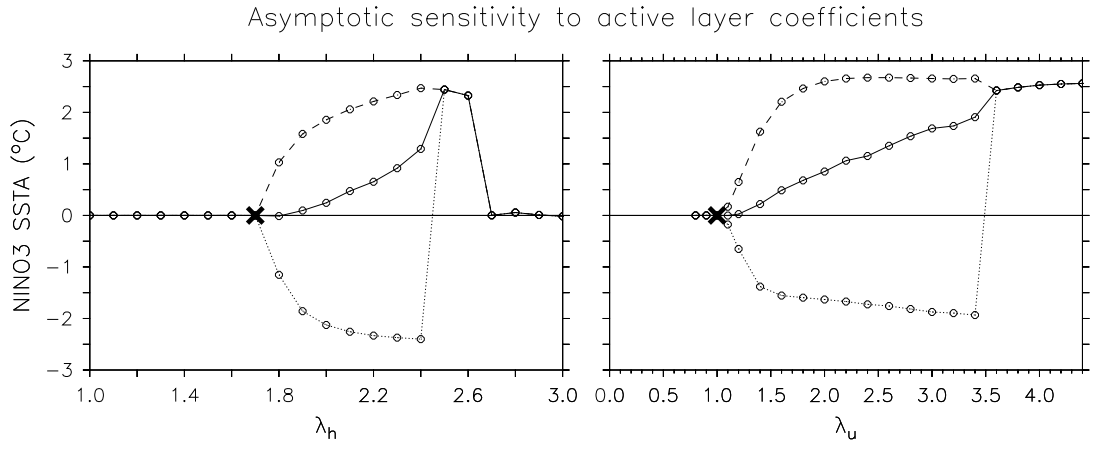

Figure 4.27: As in Fig. 4.25, but for the dependence of model asymptotic behavior on λ_h, the coefficient of thermocline depth anomalies, and λ_u, the coefficient of active layer current anomalies. Standard model corresponds to $\lambda_h = 1.7$, $\lambda_u = 1.0$.

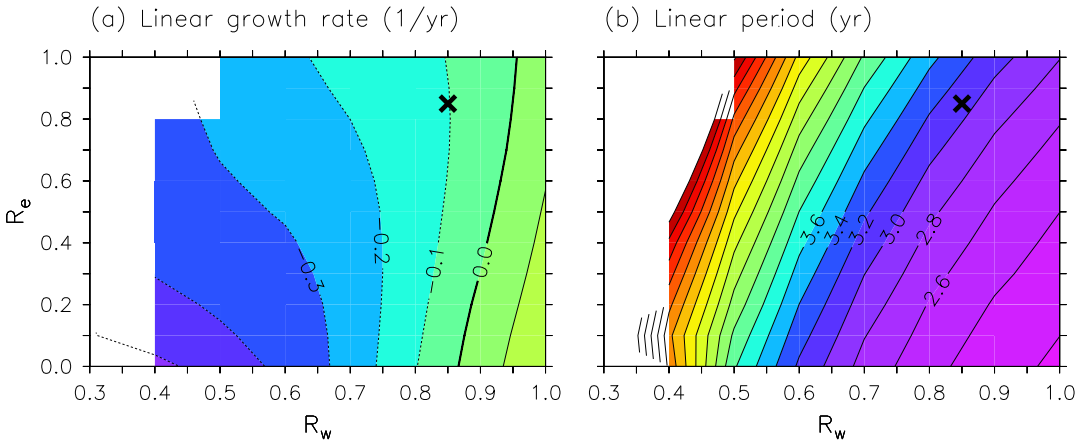

Figure 4.28: As in Fig. 4.26, but for the western and eastern boundary reflectivities R_w and R_e.

The asymptotic response is shown in Fig. 4.27, for a wider range of active layer coefficients. The dependence on these coefficients looks much like the dependence on the coupling strength shown in Fig. 4.25. Above the Hopf bifurcation, the oscillation grows more and more skewed until a permanent warm state is reached. In terms of the bifurcation structure, a 30% increase in μ is roughly equivalent to a 50% increase in λ_h (holding λ_u constant), or a 350% increase in λ_u (holding λ_h constant).

Sensitivity to boundary reflectivity

Fig. 4.28 shows the sensitivity of the linear growth rate and period to changes in the western and eastern boundary reflectivities. The behavior of the anomaly model is more sensitive to R_w than to R_e. As R_w decreases, the western boundary admits a greater zonal mass flux, which serves to recharge equatorial heat content during warm events and discharge equatorial heat content during cold events. As a result, events take longer to terminate, and so the period lengthens. The oscillations also become more stable, because the decrease in reflected feedback reduces a crucial growth mechanism during the onset of events (Battisti and Hirst, 1989). As R_e decreases, on the other hand, the period shortens slightly and the oscillations become either less damped (for $R_w > 0.7$) or more damped (for $R_w < 0.7$). There is a critical threshold for R_w, below which there are no oscillations; this threshold decreases with decreasing R_e, since the eastern boundary assists in the equatorial discharge of heat content associated with the wind stress curl.

The asymptotic sensitivity to boundary reflections is shown in Fig. 4.29. As R_w decreases below the bifurcation value near $R_w = 0.85$, the western boundary flux increases, until near $R_w = 0.4$ it finally overcomes the negative feedbacks associated with the geostrophic divergence in the interior. Beyond this point the model asymptotes to a permanent warm state, which strengthens as R_w decreases further. Decreases in the eastern boundary reflectivity R_e, though they tend to reduce the oscillation damping, have too weak an effect to destabilize the system for the standard R_w.

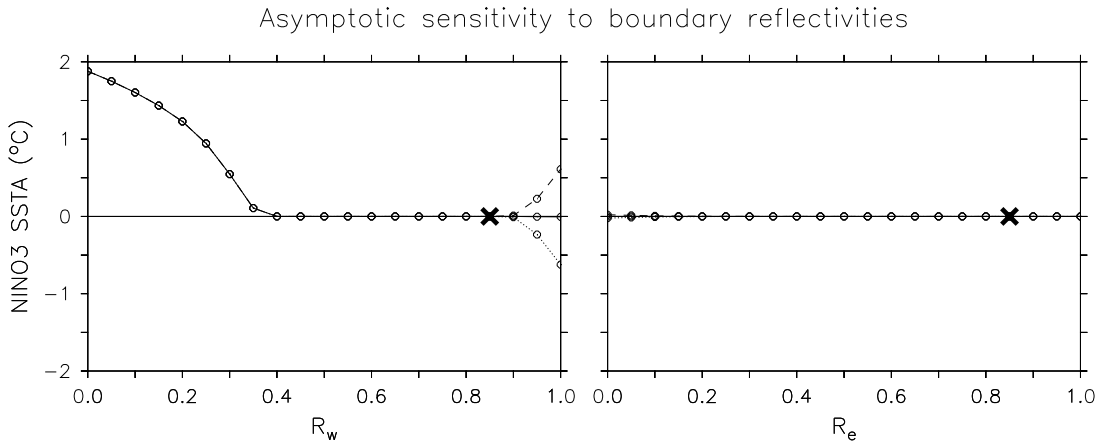

Figure 4.29: As in Fig. 4.25, but for the dependence of model asymptotic behavior on R_w and R_e, the reflectivities of the western and eastern boundaries. Standard model corresponds to $R_w = R_e = 0.85$.

4.3.3 Influence of stochastic forcing

Day-to-day weather is turbulent, so initial uncertainties in the state of the atmosphere grow exponentially in time. The saturation of these errors at small scales produces essentially random noise, which perturbs the slower climate components of the coupled air-sea system. We will therefore refer to the equilibrated chaos associated with atmospheric weather as "noise" or "stochastic forcing," and reserve the word "chaos" for use in describing ENSO behavior in the absence of such noise.

That the model is so close to the stability boundary suggests that a sustained oscillation of reasonable amplitude could be maintained by random forcing. In this section, we incorporate into the model the red noise estimate derived in Chapter 3. This forcing will parameterize the influence of highly unpredictable elements of the tropical climate system, like westerly wind events, the MJO, and day-to-day variations in tropical convection.

Fig. 4.30 shows the influence of the noise amplitude on the distribution of NINO3 SSTA. The particular noise realization is the same in all cases, except that its amplitude is changed. As the noise amplitude increases, the ENSO amplitude increases, the mean and median NINO3 SST become warmer, and the distribution of NINO3 SSTA skews more towards cold events.

The spectral character of the timeseries also changes with increasing noise amplitude. For weak noise (Fig. 4.31), the oscillation is fairly regular, with a sharp spectral peak near 3.2 yr period that is easily distinguished from red noise. Even with this very weak stochastic forcing, the oscillation exhibits large amplitude fluctuations from decade to decade, and slight variations in frequency as well. One might be tempted to infer that something about the dynamics of the system or the noise was different in year 50 than in year 55. Such a conclusion, however, would be erroneous, as both the dynamics and the noise statistics are perfectly stationary in this experiment. The temporal variations result entirely from random coincidences, in which the noise just happens to project strongly onto the system

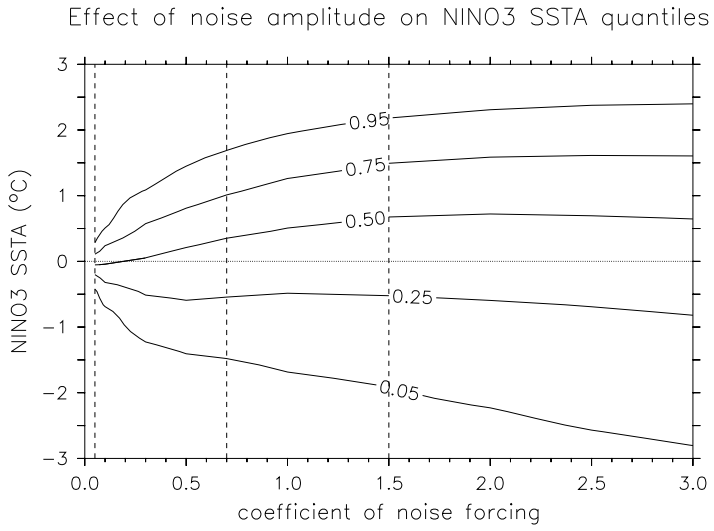

Figure 4.30: Quantiles of NINO3 SSTA (°C) from a 100 yr run forced by wind stress noise, as a function of the noise amplitude. A noise coefficient of 1.0 corresponds to the amplitude estimated from the FSU pseudostress data for 1980–1999. Dashed lines indicate the cases selected for spectral analysis.

dynamics for a time.

For moderate noise amplitude (Fig. 4.32), the spectral peak broadens and there are larger temporal variations in frequency. The time-average spectral signature of the oscillation is still readily distinguished from red noise. The peak period lengthens to 3.7 yr and a substantial short-period tail develops. Amplitude modulation is again evident within the interannual band, although it is weaker and has a shorter period than in the weak-noise case. The spectral variations for this moderate-noise case qualitatively resemble those for observed SST anomalies, shown in Chapter 2.

For strong noise amplitude (Fig. 4.33), the spectrum covers a broad range (0.8 yr to 5 yr) but is still significantly different than red noise. Though it may appear "noisier" than the cases with weaker stochastic forcing, in a sense the timeseries is also more stationary, in that the power within the interannual band shows less extreme temporal variations than before.

Perhaps the most important effect of the noise, regardless of amplitude, is that it induces large temporal variations in ENSO amplitude and frequency. This suggests that any effects of changes in the background state on ENSO may be difficult to discern if the signal-to-noise ratio is small.

4.3.4 Predictability

The skill of a deterministic climate forecast depends on two things: the quality of the forecast system, and the nature of the climate phenomenon to be forecast. A good dynamical forecast system requires a realistic numerical model and accurate initial conditions,

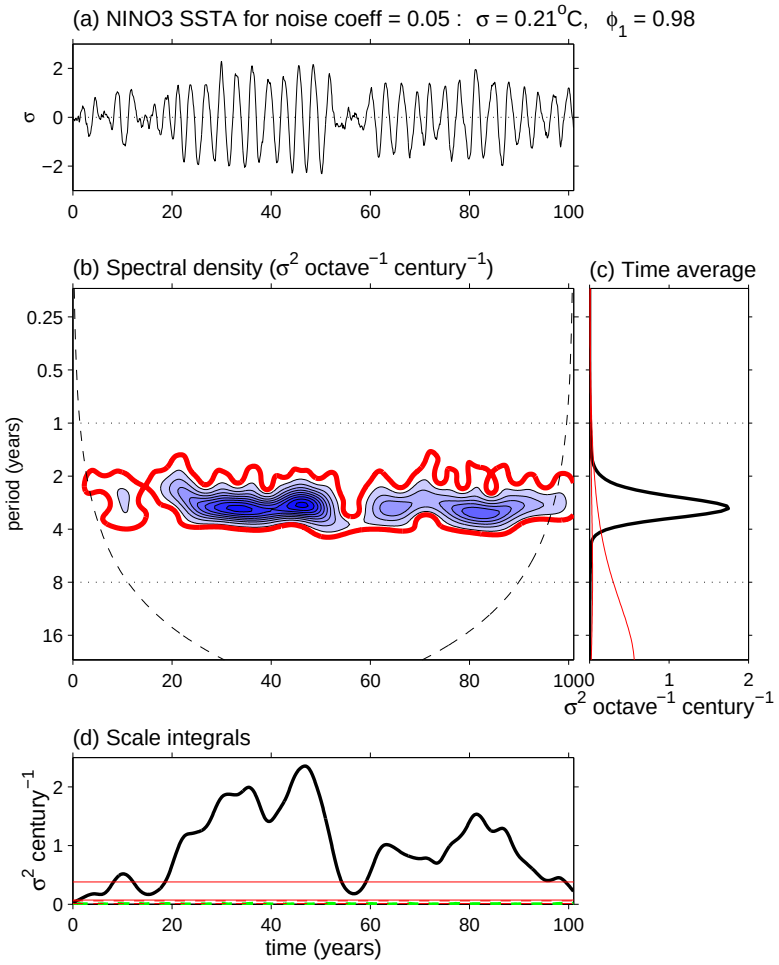

Figure 4.31: Wavelet analysis of NINO3 SST anomalies, simulated by the hybrid model with weak stochastic forcing (0.05 times the FSU estimate for 1980–1999). (a) 100-yr timeseries of standardized monthly anomalies of NINO3 SST. The standard deviation σ and lag-1 autocorrelation ϕ_1 are indicated at the top of the plot. (b) Spectral density of the timeseries, obtained by convolution with a wavenumber-6 Morlet wavelet. The base contour and contour interval are 0.5 σ^2 octave^{-1} century^{-1}. The dashed line ("cone of influence") represents twice the e-folding time for the wavelet response to a spike in the timeseries; below this line the spectral density is underestimated due to edge effects. Thick contour encloses the 95th percentile for red noise realizations with the same σ and ϕ_1 as the timeseries. (c) Time-averaged spectra. Thin lines bracket the central 90% of wavelet spectra calculated from 100-year realizations of the red noise. (d) Running variance in the 0–1 year spectral band (thick dashed) and the 1–8 year band (thick solid). Thin lines bracket the central 90% of running variances calculated from red noise.

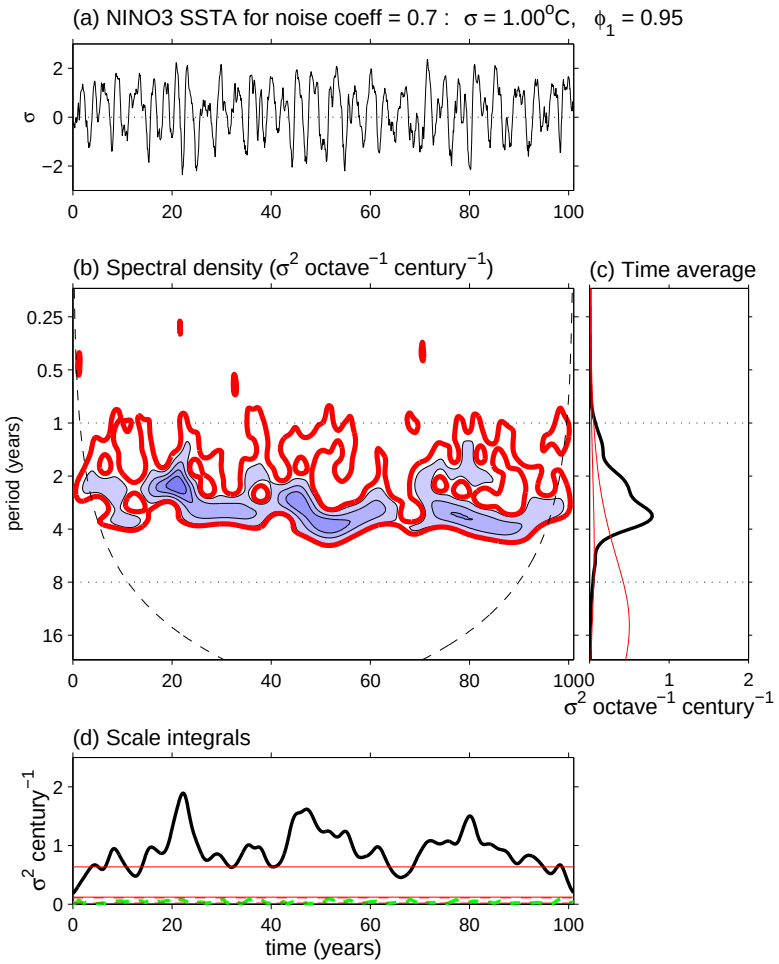

Figure 4.32: As in Fig. 4.31, but for moderate stochastic forcing (0.7 times the FSU estimate for 1980–1999).

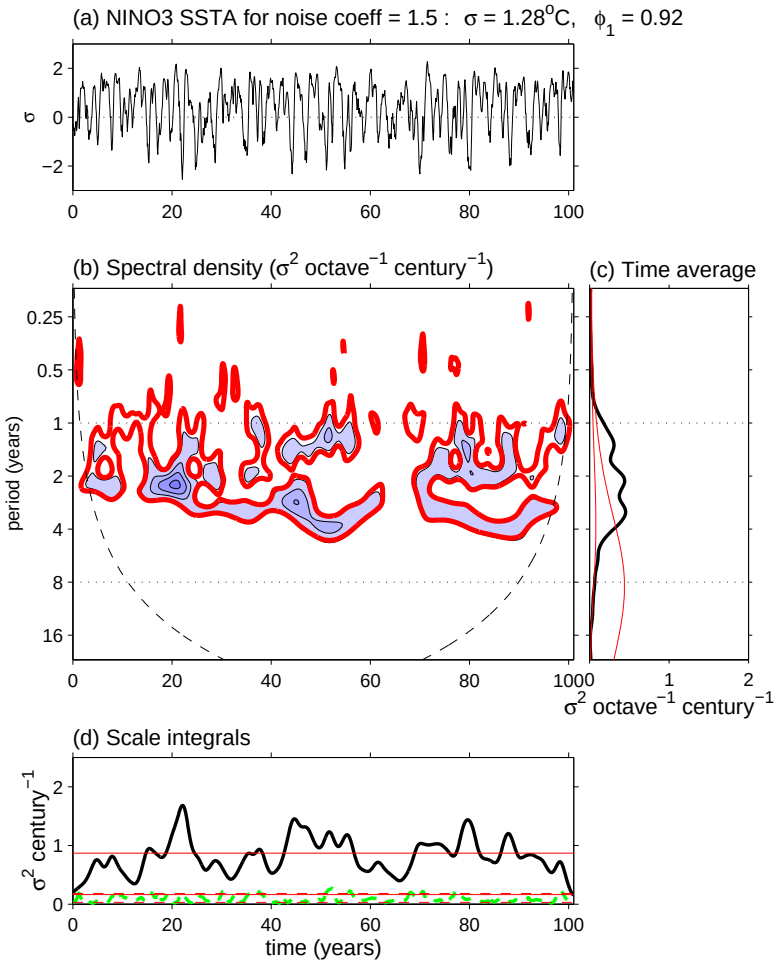

Figure 4.33: As in Fig. 4.31, but for strong stochastic forcing (1.5 times the FSU estimate for 1980–1999).

which the forecaster can control and science can work to improve. What the forecaster cannot control, however, is the climate phenomenon itself, which may have limited predictability even given a perfect forecast system. In this section we explore these natural limits in the context of the intermediate model, by examining the skill of predictions issued using a perfect forecast system and perfect initial conditions.

The nature of predictability

The predictability of ENSO depends on many characteristics of the climate system. Two of these have to do with the noise forcing. The noise *amplitude* is important because it determines the amount of randomness introduced into the system: in the extreme case that the system is simply pure noise, then a climatological forecast (historical event probabilities without reference to the initial conditions) is the best a forecaster can hope to do. The spatial and temporal *structure* of the noise are also important, because they determine the extent to which the noise projects onto the climate phenomenon of interest, i.e. they set the "effective" noise amplitude.

The *probability distribution* of the noise also affects the nature of the forecast problem. If the noise distribution is light-tailed, namely strong events are rare relative to weak events, then forecasts will fail spectacularly just prior to times when a strong noise event does, by chance, occur. Immediately *following* such an event, however, predictability may be enhanced as the system responds deterministically to the unusually strong noise perturbation and retains, for a time, the information associated with that perturbation.

The third characteristic important to ENSO predictability is the lifetime of initial information, which is related to the system dynamics. If ENSO is strongly damped and sustained only by noise, then initial information will rapidly be lost and forecasts cannot hope to improve upon the climatological forecast at long leads. On the other hand, if ENSO is so unstable that it is strongly affected by nonlinearity, then the deterministic system itself may limit predictability at long leads, through sensitive dependence on initial conditions (chaos). It would appear that the best situation for forecasters would be when ENSO is in an intermediate regime where the dynamics are linear, weakly damped and gently sustained by noise. In this case, not only would forecasts following an extreme event would be forgiving of errors in the initial conditions, but they would also yield useful information at long leads while the ENSO signal remained above the weak background noise level.

There is much debate and confusion over the nature of the observed ENSO: is the phenomenon unstable or damped, linear or nonlinear, chaotic or stochastic? Studies which have attempted to classify the system (Jin et al., 1994; Tziperman et al., 1995; Penland and Sardeshmukh, 1995; Chang et al., 1996; Flügel and Chang, 1996; Blanke et al., 1997; Neelin et al., 1998; Thompson and Battisti, 2000, 2001) suggest at least some role for each of the above. ENSO in reality may be a chameleon, changing its colors through the calendar year and from decade to decade. The control run represents a particular type of ENSO which is reasonably consistent with observations, so it is worthwhile investigating the predictability of this system. This control run will also provide a baseline for comparison with the perturbed-climate runs in Chapter 7.

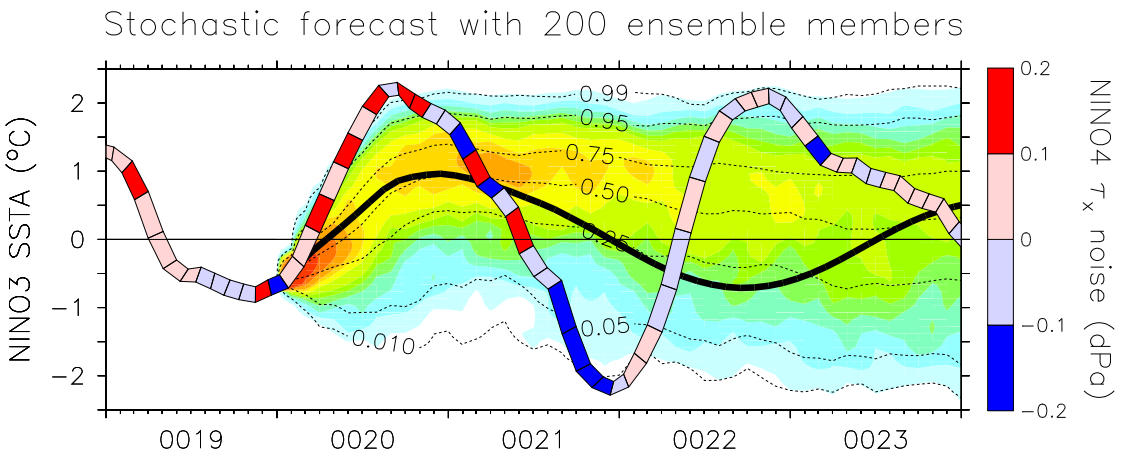

Figure 4.34: Stochastic probability forecast of NINO3 SST anomalies (°C). The stochastic control run is illustrated as a banded tube, where the colors indicate the NINO4 amplitude of zonal stress noise in that run. The control run provides the initial conditions, beginning in year 20, for 200 stochastic forecasts forced by different realizations of the noise. Contours give the fraction of forecasts colder than a given temperature; shading gives the probability density. Solid line shows the response of the model without any noise.

Stochastic probability forecast

To examine the growth of ENSO forecast errors, we perform an idealized prediction experiment. The control run is used to generate the initial conditions for an ensemble of 200 coupled forecasts. Each forecast begins with the same initial condition, which corresponds to the end of a weak cold event at year 20 in the control run. Subsequently, each ensemble member is forced by an independent realization of the noise forcing.

The resulting plume of forecasts (Fig. 4.34) illustrates the fundamental uncertainty of the stochastically driven ENSO, which cannot be reduced by improving the forecast system or initial conditions. The contours represent the cumulative distribution function (CDF) of NINO3 SSTA for the stochastic ensemble, i.e. the fraction of ensemble members colder than a given temperature. (The CDF is the integral, over temperature, of the ensemble probability distribution function (PDF)). The dashed line corresponds to purely deterministic forecast, which is the model ENSO response in the absence of noise.

One year after initialization, both the deterministic forecast and the stochastic ensemble suggest a moderate warming of the eastern Pacific. This indicates that the model was indeed predisposed at year 20 to go into a warm event. Such a warming may be amplified if the noise forcing happens to provide a series of westerly wind events in the western Pacific just after year 20, as illustrated by the striped line, which corresponds to a particular stochastic realization. This run, which is colored according to the noise-induced NINO4 zonal wind stress anomaly, apparently experienced a random series of strong westerly wind bursts during the first half of year 20, which contributed to an unusually strong warm event. The subsequent cold event, furthermore, was unusually strong due to a random series of strong easterly bursts in the latter half of year 21. Although such strong events are rare,

they can occur entirely by chance and cause a deterministic forecast to fail. Such may have been the case operationally for the very strong El Niño of 1997–98 whose amplitude was not well forecast (Landsea and Knaff, 2000), perhaps because it was affected by a series of strong westerly wind bursts in the western Pacific (van Oldenborgh, 2000) which may not have been predictable.

Faced with such situations, the best a forecaster can do is to predict the full probability distribution of system states, so that users can adequately assess the risk of extreme events. This can be done, as in the present case, by using forecast ensembles which explicitly incorporate the noise. Such a probabilistic forecast will incorporate knowledge not only of the initial conditions and deterministic dynamics, but also of the noise statistics and the dynamical system's sensitivity to that noise.

In Fig. 4.34, the spreading of the CDF contours with time corresponds to a loss of deterministic predictability, as the system is affected more and more by random events. Four years after initialization, the impact of the initial condition has been completely obscured by noise, and the stochastic ensemble settles into statistically steady fluctuations with damping balancing the noise excitation. At that point there appears to be little forecast utility left in the ensemble beyond mere climatological probabilities. Thus in the present system, the predictability of ENSO is effectively limited to less than one cycle, consistent with results from previous model studies (Goswami and Shukla, 1991; Latif and Flügel, 1991; Eckert and Latif, 1997).

What insight does the deterministic forecast (dashed line) offer into the evolution of the stochastic ensemble distribution (contours)? For the first year of the forecast, the deterministic run closely tracks the median of the stochastic ensemble, with both showing a warming relative to the equilibrium state. After this, however, the deterministic run transitions into a cold state, while the median of the stochastic runs slowly approaches its stochastic equilibrium value near 0.5°C without further fluctuation. Note that although the *individual* stochastic ensemble members are oscillating quite rapidly, most with an even shorter period and stronger amplitude than the deterministic forecast, the phase information associated with the initial conditions has been randomized away by the end of the first year. Thus the temporal phase of the deterministic run does not yield much insight into the evolution of the stochastic ensemble median or quartiles.

Clearly, if the noise amplitude is strong, then to some extent (1) the accuracy of initial conditions may be of little concern, since initial errors will quickly be overwhelmed by noise-induced perturbations, and (2) the asymptotic behavior of the unforced ENSO system (damped or chaotic) may be irrelevant, since the noise continually excites transient variability. To improve forecasts in the stochastic regime, one may have to go beyond improving the initialization and deterministic model behavior, and include an adequate representation of noise and its transient effects on error growth (Moore and Kleeman, 1996, 1997a,b, 1998, 2001).

A measure of predictability

To summarize the information in Fig. 4.34, we shall assume that the ensemble PDF of NINO3 temperature anomalies T is practically normally distributed, with a spread

characterized by its sample variance s^2:

$$s^2 \equiv \frac{N\left\langle |T - \langle T \rangle|^2 \right\rangle}{N-1} \tag{4.32}$$

where $\langle\ \rangle$ denotes the mean over all N ensemble members. For normal variables, s^2 is an unbiased estimate of the ensemble variance σ^2. For the experiment of Fig. 4.34, σ^2 is initially zero and increases with forecast lead time due to the influence of noise, eventually saturating at the climatological variance σ_c^2. An unbiased estimate of σ_c^2 is given by s_c^2, the sample variance (based on N_c ensemble members) long after initialization. The variance ratio σ^2/σ_c^2, estimated by s^2/s_c^2, is a measure of the uncertainty of a forecast relative to the maximum uncertainty associated with a climatological, or stochastically equilibrated, ensemble. This ratio has often been used in predictability studies, to quantify the "reproducibility" of model trajectories (Hayashi, 1986; Murphy, 1988; Stern and Miyakoda, 1995).

The "predictive power" (PP) of an ensemble forecast may be defined in terms of its "information content," namely the fraction of possible system states which are eliminated by the forecast. One such definition, which arises in information theory, reduces to

$$\mathrm{PP} \equiv 1 - \frac{\sigma}{\sigma_c} \tag{4.33}$$

in the case of univariate normal state vectors (Schneider and Griffies, 1999). For a stochastic forecast, like that in Fig. 4.34, the predictive power of the ensemble will decrease from one toward zero, as noise gradually degrades the information associated with the initial conditions.

The predictive power may be estimated from a given forecast ensemble, to provide an indication of the usefulness of the forecast and to summarize the information in the CDF (Fig. 4.34). A given estimate of the PP will of course differ from the true value. Under the assumption of univariate normal state vectors, however, it is possible to construct an explicit confidence interval for the PP (Appendix E). In general, the larger the ensemble, the better the estimate of the forecast variance, and the tighter the confidence interval for the PP.

Predictability as a function of time

The stochastic ensemble experiment of Fig. 4.34 illustrates the evolution of forecast uncertainty for a single initial condition. To find the "average" decay of predictability with forecast lead time, we must repeat this experiment at multiple points along the control run. In this section we shall consider only ENSO-phase-related effects on predictability, but it should be noted that seasonal effects are also important (Zebiak and Cane, 1987; Battisti, 1988; Latif and Flügel, 1991; Goswami and Shukla, 1991; Balmaseda et al., 1995; Chen et al., 1995; Barnston, 1995; Battisti and Sarachik, 1995; Penland and Sardeshmukh, 1995; Penland, 1996; Flügel and Chang, 1998).

To investigate predictability in the control run, we perform a series of ensemble forecast experiments. Every 2 months the control run is used to initialize 10 new forecasts, which are

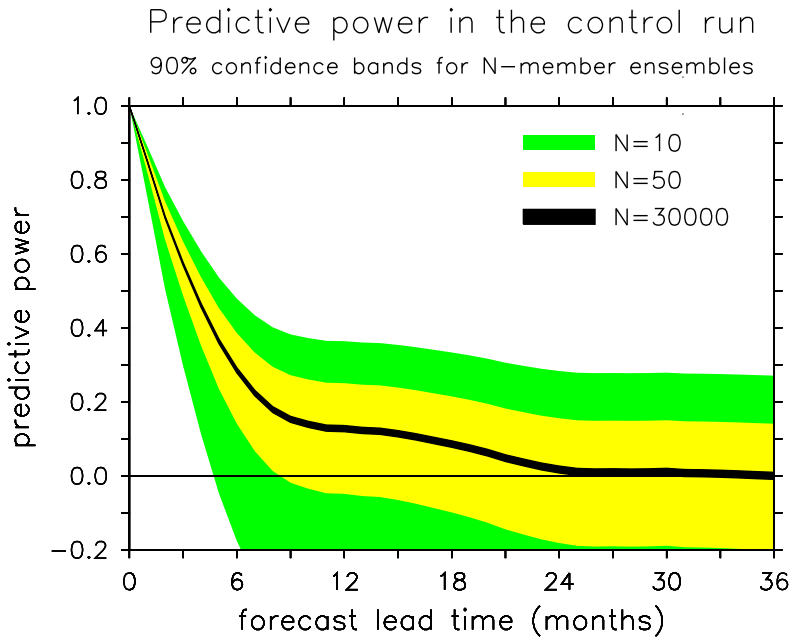

Figure 4.35: Predictability of NINO3 SST anomalies in the stochastic model, as a function of forecast lead time. Shading indicates 90% confidence bands for the predictive power (PP), corresponding to an ensemble of size 10 (green), 50 (yellow), or 30,000 (black). Where the confidence band does not include zero, the PP is greater than zero at the 5% significance level.

initially identical but subsequently diverge under the influence of different noise realizations. This forecast experiment is repeated every 2 months for 500 years, giving a total of 30,000 individual forecasts corresponding to 3,000 different initial conditions. At each lead time, an estimate s^2 of the ensemble variance is obtained by pooling the ensemble sample variance over all 30,000 forecasts. The value of s^2 at 3 years lead is then taken as an estimate s_c^2 of the climatological variance. These estimates of s^2 and s_c^2 are then used to calculate the PP (4.33) and its confidence interval (E.6).

The black band in Fig. 4.35 is the 90% confidence band for the predictability of NINO3 SST anomalies in the stochastic model, as measured by pooling the predictive power over all 30,000 forecasts. Initially, the forecast ensemble provides perfect information (PP = 1) by eliminating all uncertainty in the system state. As forecast lead time increases, the predictability decays due to the influence of noise, and at 6 months less than a third of the initial information remains. With the pooled ensemble of 30,000 forecasts, the confidence interval for the PP is very tight, and it is clear that there is useful information in the ensemble for up to two years beyond initialization.

Unfortunately, operational forecasts using coupled GCMs cannot afford anywhere near this many ensemble members; with present computing resources, a forecast ensemble of 10 is more reasonable. PP confidence bands for small ensembles, obtained by reducing the degrees of freedom in the F-distribution quantiles of (E.6), are shown for the stochastic

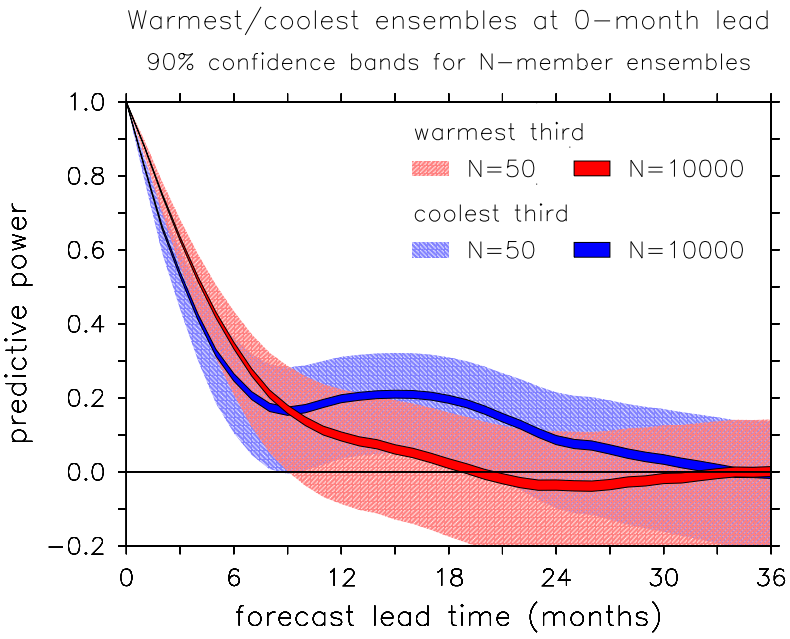

Figure 4.36: As in Fig. 4.35, but divided into forecasts belonging to the warmest and coolest terciles for initial NINO3 SSTA.

model as the lighter-colored bands in Fig. 4.35. For a 10-member ensemble, the predictive power is distinguishable from zero only during the first 5 months of the forecast; beyond this lead time, such a small ensemble cannot reliably detect the small differences between the system PDF and the climatological PDF. Increasing the ensemble size to 50 members, however, increases the precision of the forecast and extends the window of predictability to nearly 9 months.

Predictability for different initial conditions

The coupled model response to wind events is nonlinear (Figs. 4.22 and 4.23) and its stochastic evolution is skewed towards cold events (Fig. 4.30). Thus it is worth asking to what extent the predictability of the model ENSO is affected by the initial conditions of the forecast. To answer this question, the 30,000 forecasts of Fig. 4.35 are stratified according to their initial NINO3 SST anomaly, and classified as "warm starts" (top tercile) and "cold starts" (bottom tercile). Fig. 4.36 shows the evolution of the predictive power, pooled separately over warm and cold starts. With 10,000 ensemble members apiece the confidence bands are very tight, and it is clear that the forecasts from warm starts are the more reproducible during the first 9 months of the forecast. This is likely the result of nonlinearities, such as those described in Section 4.3.1, which during cold events tend to favor coupled instabilities and ruin the forecasts. At longer leads, after most of the system predictability has already been lost, the forecasts with warm starts begin going into cold events, and therefore continue to lose predictability rapidly. The cold starts, on the other hand, by this time begin entering long warm events, such that they retain

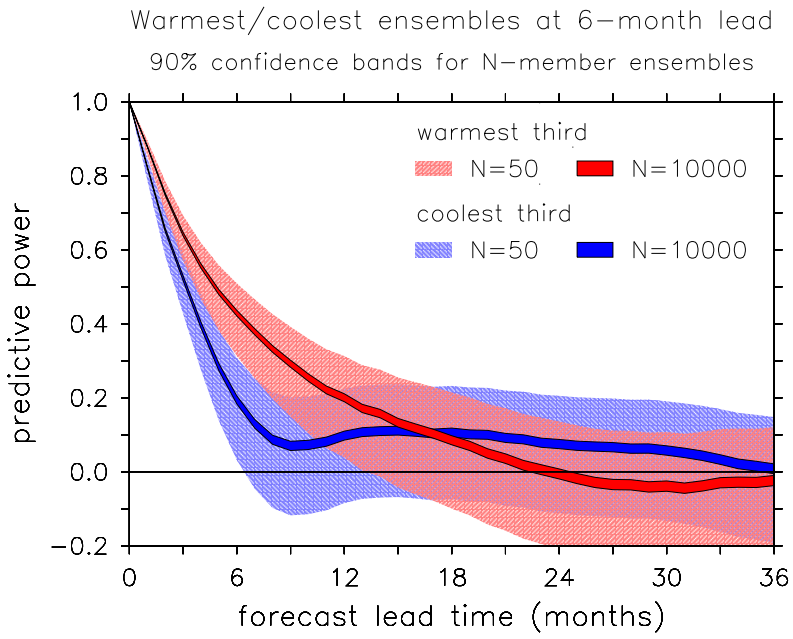

Figure 4.37: As in Fig. 4.36, but divided into forecasts belonging to the warmest and coolest terciles for ensemble-mean NINO3 SSTA at 6 months lead.

significant predictability for nearly two more years.

With an operationally feasible ensemble size of 50, the confidence bands for warm and cold starts overlap for all but the first two months of the forecast. Thus for operational forecasts, it would be hard to distinguish the predictability difference between a forecast with a warm start and one with a cold start. One important difference does emerge, however: the PP for warm starts is significant for only the first 9 months of the forecast, the PP for cold starts remains marginally significant for nearly twice as long. Thus at the 5% significance level, one *could* state that long-lead forecasts from cold starts have predictive power; but one could *not* make the same statement for warm starts.

Are warm events in the model more predictable than cold events? To answer this question, the 30,000 forecasts of Fig. 4.35 are stratified according to their ensemble-mean NINO3 SST anomaly at month 6 of the forecast, and classified as 'warming forecasts" (top tercile) and "cooling forecasts" (bottom tercile). Fig. 4.37 shows the evolution of the predictive power, pooled separately over the warming and cooling forecasts. With 10,000 ensemble members, it is clear that the warming forecasts are the more reproducible during the first year of the forecast. With only 50 ensemble members, this difference is harder to see, but with a few more ensemble members or a slightly less stringent significance test one would be able to state that there is indeed a difference in the predictability for these two types of forecasts. With 50 ensemble members the warming forecasts maintain significant PP past one year, while the cooling forecasts maintain significant PP only for about 6 months.

Thus predictability in the stochastic model does appear to be a function of the initial

condition and the evolution of the ensemble mean. In particular, ensembles which enter warm events early in the forecast tend to have higher predictability than those that enter cold events. Some of these predictability variations would be difficult to see in operationally feasible forecasts, due to the large sampling variability associated with small ensembles. Even for such small ensembles, however, it is possible to distinguish between these forecast cases by testing them against the hypothesis of no predictability: cases which start cold or go warm tend to maintain significant predictability for longer periods.

The predictability variations noted above are related to the skewness of the SST anomalies (Fig. 4.30) in the model. Due to nonlinearities, warm SSTAs tend to persist longer and are less sensitive to wind stress noise than cold SSTAs (Figs. 4.22 and 4.23), which causes warm events to be more predictable than cold events. It is important to note, however, that *observed* NINO3 SST anomalies tend to be skewed toward *warm events*, not cold events as in the coupled model. This is probably due to convective nonlinearities in the real atmosphere, which are neglected by the linear statistical wind stress model. It is likely that in the real world, the sharp peaks of warm events are less predictable than the slow troughs of cold events. Indeed, this is the case in the original Zebiak and Cane (1987) model, which includes a simple parameterization of convective nonlinearity (Samelson and Tziperman, 2001). The key points to take from Figs. 4.36 and 4.37 are that (1) there is a strong link between the predictability of a system and its dynamics, and (2) one must have a large forecast ensemble to reliably detect variations in predictability.

4.4 Summary

The purpose of this chapter has been to develop a coupled model of tropical Pacific climate, which can simulate both the annual-mean climatology and ENSO variability. The resulting intermediate-complexity model is fast, flexible, and conceptually efficient. While the model is based largely on the pioneering work of Zebiak and Cane (1987), several aspects are new. First, the atmosphere is replaced with a statistical model based on recent observations, including an estimate of the intraseasonal variability thought to play some role in observed ENSO events. Second, the ocean model is updated with more realistic boundary conditions, a more consistent advection scheme, and an improved entrainment parameterization. Finally, the ocean model is re-calibrated using newly available observations and results from recent theoretical studies.

Evaluation of the model in both forced and coupled contexts indicates that it does a reasonable job simulating the tropical Pacific climatology and ENSO variability. Some deficiencies remain, however. When the ocean model is forced with observed wind stresses, it shows more activity at short (1–2 year) timescales than do the observations. While this problem may partly be due to inaccuracies in the prescribed stress forcing, it is amplified by an unrealistically strong basin resonance of internal waves. This resonance appears to be related to the inclusion of only a single baroclinic mode in the ocean model which does not propagate downward. In the coupled context, the model SST variability tends to be displaced eastward of that in observations. This may be due to the neglect of wind speed dependence in the parameterization of surface latent heat fluxes, or to the neglect of undercurrent effects on the entrainment temperature. Finally, at large amplitude the

model SST is skewed toward cold events, instead of warm events as in the observations. This may result from the absence of convective nonlinearities in the statistical atmosphere.

Despite these limitations, the model appears realistic enough to warrant a serious investigation into its ENSO behavior. In the absence of noise, the standard version of the model responds to a wind stress perturbation with a damped oscillation and a 3 year period. This oscillation depends essentially on vertical advection in the eastern equatorial Pacific, which affects SST mainly through mean upwelling acting on the anomalous vertical temperature structure of the ocean. Zonal advection also contributes to the oscillation in the central Pacific, where anomalous currents act on the strong climatological gradients at the edge of the warm pool. These two effects show a slight phase lead relative to SST, due to delayed negative feedbacks that arrive from the western boundary in the form of reversed thermocline depth anomalies and zonal current anomalies. These feedbacks, which are associated with equatorial Rossby waves, bring about a reversal of the ENSO event and plunge the system into the opposite phase. Such behavior is consistent with current theories of ENSO evolution, with many GCMs, and with observations.

The model is only marginally stable, and can be rendered unstable by slight changes in the strength of the wind stress feedback or boundary reflectivities, resulting in a sustained, regular oscillation. In the standard (damped) model, a sustained oscillation can be maintained by turning on the intraseasonal noise portion of the atmosphere model, in which case the model spectrum fluctuates in time but is centered near a 3 year period. For realistic noise amplitude, the predictability of the model ENSO is limited to less than one cycle, with higher predictability going into warm events than cold events.

We now have a powerful tool for investigating the climate and variability of the tropical Pacific region. In remaining chapters we shall take advantage of this tool to understand how ENSO behavior is related to the tropical climatology.